Title: Maintenance of neuronal TDP-43 expression requires axonal lysosome transport

Authors: Veronica H. Ryan[1,2], Sydney Lawton[1], Joel F. Reyes[1], James Hawrot[1], Ashley M. Frankenfield[3], Sahba Seddighi[1], Daniel M. Ramos[2], Jacob Epstein[2], Faraz Faghri[2,4], Nicholas L. Johnson[2,4], Jizhong Zou[5], Martin Kampmann[6], John Replogle[1], Yue A. Qi[2], Hebao Yuan[1], Kory R. Johnson[1], Dragan Maric[1], Ling Hao[7], Mike A. Nalls[2,4], Michael E. Ward[1]

Affiliations
[1]National Institute of Neurological Disorders and Stroke, National Institutes of Health, Bethesda, MD, USA.
[2]Center for Alzheimer's and Related Dementias, National Institute on Aging, National Institutes of Health, Bethesda, MD, USA.
[3]Department of Chemistry, George Washington University, Washington, DC, USA.
[4]DataTecnica, Washington, DC, USA.
[5]National Heart, Lung, and Blood Institute, National Institutes of Health, Bethesda, MD, USA.
[6]Institute for Neurodegenerative Diseases, Weill Institute for Neurosciences, and Department of Biochemistry and Biophysics, University of California, San Francisco, San Francisco, CA, USA.
[7]Department of Chemistry and Biochemistry, University of Maryland, College Park, MD, USA.

Correspondence: wardme@nih.gov and veronica.ryan@nih.gov

Abstract
TDP-43 mislocalization and pathology occurs across a range of neurodegenerative diseases, but the pathways that modulate TDP-43 in neurons are not well understood. We generated a Halo-TDP-43 knock-in iPSC line and performed a genome-wide CRISPR interference FACS-based screen to identify modifiers of TDP-43 levels in neurons. A meta-analysis of our screen and publicly available screens identified both specific hits and pathways present across multiple screens, the latter likely responsible for generic protein level maintenance. We identified BORC, a complex required for anterograde lysosome transport, as a specific modifier of TDP-43 protein, but not mRNA, levels in neurons. BORC loss led to longer half-life of TDP-43 and other proteins, suggesting lysosome location is required for proper protein turnover. As such, lysosome location and function are crucial for maintaining TDP-43 protein levels in neurons.

Introduction
Mislocalization of transactive response DNA binding protein of 43 kDa (TDP-43) is a pathological hallmark of frontotemporal dementia and amyotrophic lateral sclerosis (FTD/ALS), two related neurodegenerative diseases, and is a co-pathology in up to 57% of Alzheimer's disease cases[1]. Mislocalization of TDP-43 includes formation of aggregates in the cytosol and/or nucleus and nuclear clearance[2, 3]. TDP-43 plays important roles in the regulation of gene expression and is critical to mRNA splicing. Nuclear loss of TDP-43 leads to increased alternative splicing events, a hallmark of TDP-43 proteinopathies[4, 5]. TDP-43 also regulates its own expression at the mRNA levels by binding to its own 3' UTR, but this autoregulation is insufficient to maintain normal nuclear expression in disease[6-8]. Whether other factors also regulate TDP-43 expression in neurons has not been systematically studied. Identification of such factors could reveal upstream disease mechanisms and potential therapeutic targets for neurodegenerative diseases.

The development of pooled CRISPR interference (CRISPRi) screens has allowed researchers to test the effect of thousands of genetic perturbations in parallel[9]. CRISPRi screens are now possible in neurons derived from human induced pluripotent stem cells (iPSCs), enabling the evaluation of the effect of gene knockdowns on various phenotypes in these iPSC-derived

neurons (iNeurons). Initial screens in iNeurons focused on survival-related phenotypes[10, 11]. More recently, FACS-based screens in iNeurons have enabled identification of modifiers of oxidative stress and peroxidized lipids[11]. Historically, a practical challenge in the application of FACS-based screens to iNeurons has been that traditional genome-wide sgRNA libraries are large (>100K sgRNAs), making it difficult to sort sufficient cells to identify phenotypes. Therefore, sub-library screens have often been used in the past, limiting the scope of genes assayed. Recently, compact dual-sgRNA CRISPRi libraries have been developed[12], setting the stage for genome-wide FACS-based screens in iNeurons.

To uncover mechanisms leading to altered TDP-43 protein levels, we endogenously tagged the TARDBP gene with HaloTag in iPSCs, thereby generating a Halo-TDP-43 knock-in iPSC line to monitor TDP-43 expression in iNeurons. Using this line, we conducted a whole genome CRISPRi FACS screen to identify modifiers of TDP-43 expression. Meta-analysis of this screen and other genome-wide CRISPRi FACS screens in iNeurons revealed common pathways shared across screens independent of the measured phenotype, enabling us to rank pathways specific for TDP-43 expression. All eight of the components of the BORC complex, which is necessary for axonal lysosome transport[13], were required to maintain neuronal TDP-43 expression. The genes encoding the 8 subunits are BORCS1 (BLOC1S1), BORCS2 (BLOC1S2), BORCS3 (SNAPIN), BORCS4 (KXD1), BORCS5 (alias LOH1CR12), BORCS6 (alias C17orf59), BORCS7 (alias C10orf32), and BORCS8 (alias MEF2BNB). Knockdown of BORC reduced TDP-43 protein, but not RNA, levels. Surprisingly, metabolic labeling proteomics revealed that loss of BORC resulted in longer turnover time of TDP-43 protein. Notably, lysosome function and location also influenced Halo-TDP-43 levels in iNeurons. Our results identify BORC as a novel modifier of TDP-43 protein levels and point to a new mechanism by which TDP-43 levels are regulated in neurons.

Results

Generation of a Halo-TDP-43 knock in iPSC line

The amount of TDP-43 expressed in neurons is tightly regulated and TDP-43 undergoes autoregulation of its own transcript levels[14] to ensure levels are maintained at appropriate levels. To visualize and quantify the amount of TDP-43 in living cells, we used CRISPR technology to endogenously tag the N-terminus of TDP-43 with a HaloTag (Figure 1A). We selected a clone with correct editing based on sequencing. In this clone, knock in of the HaloTag was heterozygous, leaving the second allele of TDP-43 intact and unedited. The lead clone displayed a normal karyotype (Figure S1A), demonstrating that there were no major chromosomal abnormalities introduced during the gene editing or subsequent clonal expansion. Imaging of iNeurons differentiated from the knock in iPSC line showed the majority of Halo signal in the nucleus, as is expected for TDP-43 localization (Figure 1B). A western blot against TDP-43 shows a shift of approximately 35 kDa in the two TDP-43 positive bands, corresponding to the molecular weight of Halo (33 kDa) (Figure 1C, S1B). Knocking down TDP-43 using CRISPRi reduced the amount of both tagged and untagged TDP-43 compared to a non-targeting (NT) sgRNA (Figure 1C-D). Expression of Halo-TDP-43 was roughly 60% of endogenous TDP-43, indicating that the Halo-tagged protein is either not transcribed or translated as efficiently as untagged protein, or the protein is degraded more readily.

CRISPRi FACS screen identifies modifiers of Halo-TDP-43 levels in iPSC derived neurons

To identify upstream modifiers that alter TDP-43 levels, we performed a genome-wide CRISPRi FACS-based screen in both Halo-TDP-43 iPSCs and iNeurons differentiated from our Halo-TDP-43 iPSC line using a dual sgRNA library, enabling 1000x coverage of the genome by sorting only 20 million iNeurons[12]. We sorted for cells highly expressing the GFP sgRNA marker and then sorted the cells containing the lowest 25% of Halo signal into one tube and the cells

103 containing the highest 25% of Halo signal into another (Figure 2A). sgRNAs targeting the
104 TARDBP transcription start site decreased Halo-TDP-43 levels in both the iPSC and iNeuron
105 screens (Figure 2B and S2A, Tables S2 and S4), indicating that our screen successfully
106 identified genes that decrease TDP-43 levels. Non-targeting guides are clustered in the middle
107 of the rank plot for each screen, showing that gene knockdown is needed to alter Halo-TDP-43
108 levels (Figure 2B and S2A). Among genes whose knockdown decreases Halo-TDP-43 levels,
109 we identified all eight components of the BORC complex, which regulates anterograde
110 lysosome transport in axons as hits in the iNeuron, but not the iPSC screen (Figure 2B-C and
111 S2A, Tables S2 and S4). Knockdown of genes related to mitochondrial function also decrease
112 Halo-TDP-43 levels (Figure 2C and S2B). Further, we identified genes whose knockdown
113 increases Halo-TDP-43 levels, including genes involved in RNA processing (Figure 2D and
114 S2C, Tables S1 and S3). In comparing the top GO terms associated with genes that increase or
115 decrease Halo-TDP-43 levels, we found only one hypergeometric test (HGT) term associated
116 with both the neuron and iPSC screens, nonsense mediated decay (NMD) independent of the
117 exon junction complex (EJC), although it is associated with increased Halo-TDP-43 levels in
118 iNeurons and decreased Halo-TDP-43 levels in iPSCs (Figure S2D-G). Thus, our hits are cell-
119 type specific.
120
121 *Meta-analysis of open-access FACS CRISPRi screen data identifies common and novel*
122 *fluorescence modifiers*
123 CRISPRBrain (https://crisprbrain.org/) contains datasets from many CRISPRi and CRISPRa
124 screens on different cell types examining various phenotypes. We identified three FACS-based
125 CRISPRi screens on iNeurons that identify modifiers of reactive oxygen species (CellRox) and
126 lipid peroxidation (Liperfluo) using fluorescent indicators[11] and tau aggregates[15]. We performed
127 an unbiased fixed effects meta-analysis of these screens with our Halo-TDP-43 screen to
128 determine if there were any common hits across screens. These common hits across multiple
129 screens may be real hits that simultaneously change TDP-43 and alter ROS-levels, lipid
130 peroxidation, or tau aggregation; however, they may also be “false-positives” that are altering
131 general proteostasis, general cellular stresses, or neuron differentiation, where phenotypes
132 examined in these screens are a secondary or indirect effect of knockdown. Interestingly,
133 comparison of z-scores between screens shows many genes that either positively or negatively
134 regulate both our screen and the CRISPRBrain screens (Figure 3A-F). With the increased
135 power from the multiple screens, we were able to identify novel hits that were underpowered
136 previously (Figure 3A-F). Genes were considered “hits” if they were novel with directionality
137 (either up or down) compared to the total population (the average of the hits in the
138 CRISPRBrain screens). For the Halo-TDP-43 screens, genes were filtered by a LFC of 1 or -1
139 compared to the total population. We performed GO analysis on common hits from the meta-
140 analysis across screens and found enrichment in many interesting categories, including
141 ubiquitination, neddylation, autophagy, protein targeting, cell division/differentiation, and
142 cytoskeletal related terms (Figure S3A-F). On the other hand, some hits, like the BORC
143 components, seem to be specific to our Halo-TDP-43 screen, so we chose to focus downstream
144 analysis primarily on these hits that uniquely regulate TDP-43 biology. While this analysis
145 provides a level of validation of our screen results, we picked genes from select categories to do
146 a secondary, microscopy-based screen to further validate their effect on TDP-43 levels.
147
148 *Validation of screen hits narrows in on BORC as a modifier of TDP-43 levels*
149 We cloned single sgRNA plasmids for 59 genes (Table S5) that either increased or decreased
150 Halo-TDP-43 in iNeurons but not in iPSCs. sgRNAs were transduced into iPSCs individually,
151 followed by differentiation of iPSCs into iNeurons. We used automated microscopy and analysis
152 to visualize and quantify the Halo-TDP-43 signal in cells after each gene knockdown (Figure

153 4A). 34 of 59 (58%) tested genes altered Halo-TDP-43 levels in the microscopy validation
154 (Figure 4B-G, S4A-D, Table S5). For every gene tested except one, we observed a simple
155 increase or decrease in Halo-TDP-43 levels without an obvious change in Halo-TDP-43
156 localization (Figure 4B). Since we used a single sgRNA plasmid for validation and not the dual
157 guide plasmid used in the screen, some of the genes that did not pass this stage of validation
158 may not have had sufficient gene knockdown in the validation to elicit the effect observed in the
159 screen. However, we were interested primarily in the genes whose knockdown had the
160 strongest effect on Halo-TDP-43 levels. To determine if results from Halo-TDP-43 expression
161 assays also applied to endogenous, untagged TDP-43 levels, we selected 22 genes from
162 different groups in our list that passed Halo validation and performed immunofluorescence
163 microscopy for endogenous (untagged) TDP-43 (Figure 4D-G, 5A-B, S4E-F, Table S5). Of
164 these, 18 (82%) gene knockdowns showed changes in endogenous TDP-43 levels (Figure 4D-
165 G, S4E-F, Table S5). However, many gene KDs, particularly genes involved in ubiquitination
166 and m6A RNA methylation, changed untagged TDP-43 levels in the opposite direction as they
167 change Halo-TDP-43 levels (Figure 4D-G, Table S5). We posit that this Halo-untagged
168 difference may be due to inherent destabilization of the HaloTagged TDP-43. KD of BORC
169 subunit genes changed TDP-43 levels in the same direction for both Halo imaging and
170 immunofluorescence (Figure 5A-B). To rule out the possibility of neighboring gene or off-target
171 effects of CRISPRi, as has been reported previously[16], we examined the impact of BORC
172 knockout (KO) on endogenousTDP-43 levels. Using the pLentiCRISPR system, which
173 expresses the sgRNA of interest on the same plasmid as an active Cas9[17], we found that KO of
174 BORCS7 using two different sgRNAs decreased TDP-43 levels by immunofluorescence (Figure
175 5C-D). Because of the known relationship between lysosomal dysfunction and FTD/ALS
176 pathophysiology[18-24], we focused on the relationship between TDP-43 levels, lysosomal biology,
177 and BORC.
178
179 *Maintenance of neuronal TDP-43 requires active and neuritically localized lysosomes*
180 As lysosomes are the primary recycling center of the cell, breaking down macromolecules into
181 their subunits, we first asked whether lysosome activity was required to maintain TDP-43 levels
182 in iNeurons as has been observed in other cell types[25, 26]. We treated Halo-TDP-43 neurons with
183 various drugs that disrupt distinct processes in the lysosome pathway and asked if Halo-TDP-43
184 levels changed. Chloroquine (decreases lysosomal acidity), CTSBI (inhibits cathepsin B
185 protease), ammonium chloride (NH_4Cl, inhibits lysosome-phagosome fusion), and GPN
186 (ruptures lysosomal membranes) all consistently decreased Halo-TDP-43 levels, while
187 Bafilomycin A1 (BafA1, prevents lysosomal acidification and fusion with autophagosomes),
188 LLOME (causes lysosomal membrane rupture), and apilimod (PIKfyve inhibitor) did not cause
189 changes in Halo-TDP-43 levels (Figure 6A-B, S5A-C). The varied mechanisms of action of
190 these drugs indicated that many lysosomal perturbations could alter TDP-43 levels. Further, two
191 protein translation inhibitors, anisomycin and cycloheximide (CHX) also decreased Halo-TDP-43
192 levels (Figure 6A, S5B).
193
194 Having shown that functional lysosomes are required to maintain Halo-TDP-43 levels, we next
195 tested the role of lysosome location in iNeurons. As the BORC complex is required for
196 anterograde movement of lysosomes within axons of neurons[13, 27], we first asked whether Halo-
197 TDP-43 is transported on lysosomes. Our previous work showed that mRNA transport granules
198 can be transported on lysosomes and that overexpressed TDP-43 co-trafficked with lysosome-
199 associated transport granules[28]. Indeed, in comparing motile Halo-TDP-43 with static Halo-TDP-
200 43 in neurites, we found that motile TDP-43 was most often associated with lysosomes, not
201 mitochondria (Figure 6C-D). Intriguingly, upon restricting lysosomes to the soma by knocking

202 down a BORC subunit, we find that the fraction of motile Halo-TDP-43 in the periphery is
203 reduced (Figure 6E, S5D).
204
205 *TDP-43 mRNA levels are unchanged upon BORC KD*
206 We next asked whether TDP-43 RNA levels were also changed. Using qPCR, we found TDP-43
207 mRNA levels were unchanged or slightly increased upon BORCS6 KD (Figure 7A, S6A). As
208 expected, we observed statistically significant reduction of TDP-43 mRNA upon TDP-43 KD via
209 CRISPRi (Figure 7A, S6A). We then performed total RNA sequencing of BORCS6 KD iNeurons.
210 While BORCS6 mRNA levels were reduced by ~50% (Figure 7B), no change in TDP-43 mRNA
211 levels occurred (Figure 7C), indicating that loss of BORC likely decreases TDP-43 protein levels
212 independent of TDP-43 transcript expression.
213
214 As loss of BORC drastically changes the axonal transcriptome, particularly for mitochondrial
215 genes[29], we wondered what the effect of BORC KD would be on the whole cell transcriptome.
216 We found that NT and BORCS6 KD samples were substantially separated on a PCA plot, with
217 over 90% of the variability between the samples being explained by a single principal
218 component (Figure S6B). We found 98 upregulated genes and 139 downregulated genes
219 (Figure 7D) in BORCS6 KD neurons. GO analysis revealed an enrichment of terms related to
220 neuron development and axon outgrowth (Figure 7E). As loss of TDP-43 can cause splicing
221 changes and the inclusion of cryptic exons[30-32], we asked whether BORCS6 KD decreased
222 TDP-43 levels sufficiently to induce inclusion of cryptic exons[33, 34]. We did not observe an
223 increase in expression of cryptic exons in genes that are commonly mis-spliced in iPSC-derived
224 neurons after TDP-43 loss, including STMN2 and UNC13A. As such, BORCS6 KD does not
225 reduce TDP-43 protein levels sufficiently to cause functional loss of splicing repression. As
226 TDP-43 alternative poly adenylation (polyA) contributes to TDP-43 autoregulation and levels[14],
227 we asked whether BORCS6 KD changed polyA site usage using REPAC[35]. We found many
228 sites changed upon BORCS6 KD (Figure S6C), with these genes relating to GO Biological
229 Process terms like splicing, catabolism, and transport/localization (Figure S6D-E). However, we
230 did not observe any changes in TDP-43 polyA site usage upon BORCS6 KD (Figure S6C), so
231 alternative polyA cannot explain the changes in TDP-43 protein levels.
232
233 *TDP-43, like the proteome, shows longer turnover time in BORC KD neurons*
234 As loss of BORC prevents the transport of lysosomes to axons[27, 29] and mRNAs can be
235 transported on lysosomes to the periphery[28], we speculated that TDP-43 levels could be
236 decreased in BORC KD iNeurons due to decreased axonal translation of TDP-43 mRNA. Using
237 a TDP-43 mRNA N-terminally tagged with SunTag epitopes and with PP7 stem loops after the
238 3' UTR, we used microscopy to quantify the co-localization of TDP-43 new protein synthesis
239 (SunTag signal) with mRNA (PP7-coat protein signal)[36]. Surprisingly, we did not observe a
240 change in TDP-43 translation (Figure S7A). As such, we hypothesized that loss of BORC might
241 alter TDP-43 protein degradation rather than its synthesis. To test this hypothesis, we
242 performed dynamic stable isotope labeling by amino acids in cell culture (dSILAC) to measure
243 protein half-lives as well as whole neuron proteomics to measure protein abundances in
244 BORCS6 KD and non-targeting iNeurons. We found that TDP-43 total protein levels are
245 decreased in BORCS6 KD neurons (Figure 8A), further validating our earlier microscopy
246 findings. We observed a similar trend for many proteins in the proteome, with more proteins
247 showing decreased abundance than increased (Figure 8B). Interestingly, TDP-43 shows longer
248 half-life in BORCS6 KD neurons compared to the NT guide (Figure 8C), suggesting that protein
249 degradation is potentially decreased in BORC KD iNeurons. We observed similar results for the
250 total proteome, with many proteins showing longer turnover at day 7 in BORCS6 KD neurons
251 compared to NT neurons (Figure 8D-E). Longer half-lives were also observed in d15 neurons
252 although the changes in both abundance and half-life were reduced (Figure S7B-E), suggesting

253 the neurons may be better able to compensate for the loss of BORC at later time points. In
254 comparing the KEGG and REACTOME terms shown as enriched in our proteins with longer
255 turnover times in BORCS6 KD neurons (Figure 8F, S7F) to the mRNAs whose localization is
256 altered in BORC KO neurons[29], we observe many of the same categories are enriched,
257 including ribosome and biosynthetic pathways. We further queried our data for posttranslational
258 modifications (PTMs). We were able to identify 1333 phosphorylation sites. No PTMs were
259 identified on TDP-43 at either time point, so PTM enrichment may be needed to query the role
260 of PTMs in regulating the change in TDP-43 half-life with BORCS6 KD. We were able to detect
261 10 proteins with significantly changed phosphosites upon BORCS6 KD: KRI1 and RALY have
262 phosphosites increased upon BORCS6 KD while OXSR1, ELAVL4, MAP4, ADD2, CSNK2B,
263 FIP1L1, and RSF1 have phosphosites decreased upon BORCS6 KD at d7 (Figure S7G). At
264 d15, only BASP1 showed a significantly decreased phosphosite (Figure S7H). interestingly,
265 ADD2, CSNK2B, MAP4, OXSR1, and RALY are detected to have differential phosphorylation
266 and increased half-life, suggesting these phosphosites may contribute to regulation of the
267 turnover of these proteins. As TDP-43 and the proteome show similar effects of BORCS6 KD on
268 protein half-life, iNeurons are likely in steady state and making as much new heavy protein as
269 they are degrading the light protein. As such, protein translation or protein degradation could be
270 reduced. Although we did not observe a change in TDP-43 translation in our SunTag
271 experiment, it may not be accurately reflecting the translation levels of TDP-43 due to the
272 experimental necessity of over-expressing tagged TDP-43. As such, BORC may be affecting
273 TDP-43 protein levels through a complicated mechanism.
274
275 **Discussion**
276 CRISPRi screens are powerful tools to identify novel pathways regulating cellular functions.
277 Here, we use a CRISPRi FACS screen to identify the lysosome transport complex, BORC, as a
278 modifier of TDP-43 protein, but not RNA, levels. A screen in iPSCs confirms that BORC
279 specifically acts on TDP-43 in iNeurons. Additionally, we made use of publicly available
280 CRISPRi screen data to perform a meta-analysis. This meta-analysis identified common
281 pathways across screens, enabling us to focus on TDP-43-specific hits. Common pathway hits
282 across screens involve genes related to ubiquitination, neddylation, cell division/differentiation,
283 and RNA modification. We think these pathways are related to protein level homeostasis in
284 iNeurons, and our findings suggest a general utility of meta-analysis of novel screens in the
285 context of published screens to prioritize hits for follow-up and identify phenotype-specific
286 pathways.
287
288 Knockout of individual BORC subunits impairs lysosomal transport, leading to lysosomal
289 depletion in axons and altered transport of transcripts that hitchhike on lysosomes to the
290 periphery[13, 27-29, 37, 38]. We initially hypothesized that loss of BORC would reduce neuritic
291 translation of TDP-43. However, the lack of effect of BORC loss on TDP-43 mRNA or translation
292 led us to focus on the role of lysosomes as a mechanism for how BORC affects TDP-43 protein
293 levels. As knockout of BORC subunits is known to alter lysosomal lipid metabolism, lysosomal
294 content, size, and lead to decreased autophagic flux[39-42], we asked whether BORC loss altered
295 TDP-43 half-life. We found that BORC loss leads to longer half-lives of TDP-43 and many other
296 proteins. Although TDP-43 is degraded by autophagy, and thus lysosomes[25, 26], this change in
297 TDP-43 half-life due to lysosomal positioning has not been previously observed. As lysosomes
298 can be active in axons[43], this slower turnover of TDP-43 may imply that lysosomes degrade
299 proteins in axons and are important for maintaining axonal homeostasis locally. Further work is
300 needed to better understand this counterintuitive mechanism. TDP-43 protein levels are also
301 decreased by lysosome-inhibiting drug treatments, further demonstrating the requirement of
302 active and properly localized lysosomes for maintenance of TDP-43 levels. Interestingly, the
303 decreased amount of TDP-43 in iNeurons upon BORC KD was insufficient to cause inclusion of

304 cryptic exons which have been observed in models of TDP-43 loss of function[14, 30, 31, 33]. It is
305 possible that we did not observe cryptic exons simply because the levels of TDP-43 loss were
306 insufficient to induce alternative splicing (in our hands, TDP-43 KD via CRISPRi results in ~20%
307 of TDP-43 remaining, while BORC KD results in ~60% of TDP-43 remaining in iNeurons).
308 Alternatively, the longer half-life of TDP-43 due to BORC KD affects cryptic exon inclusion; more
309 work is needed to examine this possibility.
310
311 Defects in lysosome function and intracellular transport are associated with FTD/ALS[18, 44]. Our
312 studies raise the possibility that lysosomal dysfunction is an upstream actor exacerbating TDP-
313 43 loss of function phenotypes in disease. In this scenario, lysosomal mislocalization drives
314 TDP-43 loss, which might further disrupt its autoregulation in disease. Interestingly, BORC KO
315 in mice leads to neonatal death[37, 38] and mutations in BORCS8 cause infantile
316 neurodegeneration[45]. While these neurodegeneration-causing BORC mutations reduce
317 anterograde lysosome transport[45], TDP-43 levels have not been studied in patients with this
318 disorder. Thus, we speculate that patients have altered TDP-43 levels, which could be sufficient
319 to contribute to the observed neurodegeneration. As we were unable to detect cryptic exon
320 formation in our BORC KD neurons, this potential TDP-43 loss of function in BORC patients
321 may not lead to cryptic exon pathology observed in FTD/ALS patient tissue, so further work
322 would be needed to understand the role of this intermediate TDP-43 loss in patients.
323
324 As TDP-43 pathology is associated with both loss and gain of function effects[6, 46, 47],
325 understanding the pathways that lead to altered TDP-43 levels is crucial to identifying effective
326 therapeutic targets for neurodegeneration. At the same time, the more specific these pathways
327 are for TDP-43, the less likely treatments targeting these pathways will cause unwanted off-
328 target effects. We demonstrate that CRISPRi screens are a powerful method to identify these
329 specific pathways. While we did not identify genes that specifically affected TDP-43 localization
330 in iNeurons, the identified genes and pathways that specifically alter TDP-43 levels, like BORC
331 subunits, will enable us to interrogate ways to change TDP-43 protein levels as potential
332 therapies. Additionally, as more screens are performed and can be added to meta-analyses, we
333 will gain further insight into non-specific pathways affecting protein levels and thus are unlikely
334 to be effective therapeutic targets to specifically hit targets. In conclusion, these results provide
335 important insight into the pathways affecting TDP-43 levels in neurons.
336
337 **Methods**
338 *iPSC culture and neuron differentiation*
339 Procurement and use of WTC11 cells from the Coriell cell repository followed all policies
340 of the NIH Intramural research program. WTC11 cells were derived from an apparently healthy
341 30-year-old male. iPSC culture was performed following previously described protocols[48].
342 Briefly, iPSCs were grown in Essential 8 Medium (Thermo Fisher Scientific, A1517001) on
343 tissue culture plates that had been coated with Matrigel (Corning, 354277). Medium was
344 replaced daily or as needed. Accutase (Thermo Fisher Scientific, A1110501) was used to
345 dissociate cells for passaging as single cells. 50 nM Chroman-1 (MedChemExpress, HY-15392)
346 was added to promote survival after thaw and accutase treatment, until cell colonies had
347 expanded to at least 4-5 cells/colony. The iPSCs used here were previously engineered to
348 express mouse neurogenin-2 (mNGN2) with a doxycycline inducible promoter for neuronal
349 differentiation (i11w-mN)[49]. Many experiments used a line that additionally expressed a
350 catalytically inactive dCas9 fused to a KRAB transcriptional repression domain for CRISPRi
351 knockdowns[10]. These engineered cells containing dCas9 are referred to here as i11w-mNC
352 iPSCs.
353 iNeuron differentiation and culture was performed following previously described
354 protocols[48]. Briefly, on day 0 of neuronal differentiation, iPSCs were passaged with accutase

355 and plated on Matrigel-coated tissue culture plates. iPSCs were plated in induction media
356 (knockout DMEM/F12 media (Life Technologies Corporation, #12660012) supplemented with
357 N2 supplement (Life Technologies Corporation, 17502048), 1x GlutaMAX (Thermo Fisher
358 Scientific, 35050061), 1x MEM nonessential amino acids (NEAA) (Thermo Fisher Scientific,
359 11140050), 50 nM Chroman-1, and 2 µg/mL doxycycline (Clontech, 631311)). Media was
360 changed daily. On day 3 of neuronal differentiation, cells were passaged with accutase and
361 plated on tissue culture plates that were coated with poly-L-ornithine (Sigma-Aldrich, P3655).
362 Cells were plated in maturation media (BrainPhys media (Stemcell Technologies, 05790)
363 supplemented with B27 Plus Supplement (Thermo Fisher Scientific, A3582801), 10 ng/mL
364 BDNF (PeproTech, 450-02), 10 ng/mL NT-3 (PeproTech, 450-03), 1 µg/mL mouse laminin
365 (Sigma, L2020-1MG), 50nM Chroman-1 (MedChem Express, HY-15392), and 2 µg/mL
366 doxycycline (Clontech, 631311)). Half-media changes were performed every other day or every
367 3 days. Unless otherwise specified, all experiments were performed on day 7 neurons.
368
369 *HaloTag knockin*
370 1 million iPSCs were transfected with premixed 20 µg Alt-R™ A.s. Cas12a (Cpf1) V3
371 (IDT # 1081068), 200 pmol crRNA 5'-GGAAAAGTAAAAGATGTCTGAAT (IDT), and 10 µg
372 knockin (KI) plasmid donor (gene-synthesized and cloned into pUC57 by Genscript; synthesized
373 sequence contains HaloTag coding sequence inserted immediately downstream TDP-43 start
374 codon ATG and flanked by 400 bp left and right homology arms) using Nucleofector 4D with
375 buffer P3 and program CA-137 (Lonza) and then plated onto one well of rhLamin521 (Thermo)
376 coated 6-well plate with StemFlex, RevitaCell (Thermo) and HDR enhancer V2 (IDT).
377 Transfected cells were cultured in 32˚C incubator for 3 days before moving to 37˚C incubator,
378 and fresh medium was changed daily after transfection. One week after transfection, the iPSCs
379 were live stained with Oregon Green (Promega #G2801) following the manufacturer's protocol.
380 Positive cells were sorted into 96-well Matrigel-coated plate at 1 cell/well with 100 µl/well
381 StemFlex and 1x CloneR2 (Stem Cell Technologies). 10-12 days later, single-cell clones were
382 picked and KI clones were confirmed by 5'-KI and 3'-KI junction genomic PCR (5KI-F: 5'-
383 ATCGACTGGGACCTATCACG, 5KI-R: 5'-GCGTACCCTCGATAAAAACG; 3KI-F: 5'-
384 GAGACCTTCCAGGCCTTCC, 3KI-R: 5'- TCTACAATCCCCAGTTTCCA). Heterozygous KI
385 clones were further identified by the presence both non-KI and KI allele using primers
386 recognizing homology arms (WT-F: 5'- GACGCATCATAAGCCTTCAG, WT-R: 5'-
387 CCATGGATGAGACACACACC). Both non-KI and KI alleles were subject to Sanger sequencing
388 to exclude heterozygous KI clones with indels in non-KI alleles.
389
390 *Halo-TDP-43 CRISPRi FACS screen*
391 Approximately 50 million Halo-TDP-43 iPSCs were transduced with a whole genome
392 dual guide library[12] to a titer of approximately 70% in E8 with Chroman 1. The next day, the
393 media was changed to E8 without chroman 1. The next day, iPSCs were split onto new Matrigel
394 coated plates in E8 with chroman 1. The day following the split, iPSCs were treated with 8
395 µg/mL puromycin in E8 Chroman 1 to select for cells expressing an sgRNA. After selection,
396 cells were split and differentiated into neurons following the standard protocol above. Some
397 cells were maintained as iPSCs for the iPSC screen. On day 3 post dox induction, neurons were
398 split onto final PLO-coated plates. On day 7 post dox induction, cells were split for FACS. Cells
399 were stained with 200 µg/mL Halo Ligand 646 (Promega HT1060) for 15 minutes in appropriate
400 media. Papain solution (Worthington LK003176) was prepared by adding 20 mL TrypLE without
401 phenol red (Gibco 12604-013) to one vial of papain and placing it at 37˚C for 10 minutes.
402 Neurons were washed with PBS and then washed twice with PBS with 0.5 mM EDTA.
403 Papain/TrypLE was added to cells for 1-2 minutes at 37˚C. Papain was removed without
404 disturbing the neuron sheet and trituration solution (Neuron culture media, 10 µM ROCK
405 inhibitor, and one vial of DNAse freshly dissolved) was added to cells before transferring them

406 to a conical tube. Cells were pipetted 3-10 times in the conical tube until cell clumps were gone.
407 PBS was added to cells and cells were pelleted by centrifugation at 200 xg for 5 minutes.
408 Neurons were resuspended in 1 mL Papain Inhibitor Media (27 mL trituration media with 3 mL
409 Papain inhibitor) and incubated for 5-10 minutes. Cells were again pelleted by centrifugation at
410 200 xg for 5 minutes and resuspended in cell culture media before transferring cell suspension
411 into a 5 mL collection 12x75 mm polypropylene FACS tube with 35-40 µm strainer cap. Cells
412 were kept on ice until FACS was performed. Cells were sorted using the MoFlo Astrios cell
413 sorter (Beckman Coulter), with Summit software (Beckman Coulter) to setup a sorting template.
414 GFP positive cells were detected using the 488 nm laser excitation, and 520/30 nm filter for
415 capturing signal emission. Halo was detected using 640 nm laser excitation and 675/30 nm filter
416 for emission. The cells were first gated on GFP expression, which served as a highly expressing
417 co-expression marker for sgRNA, and then gated on Halo expression, as follows. Four groups
418 were collected from the FACS session: the bottom 25% of iPSCs expressing Halo-TDP-43, the
419 top 25% of iPSCs expressing Halo-TDP-43, the bottom 25% of neurons expressing Halo-TDP-
420 43, and the top 25% of neurons expressing Halo-TDP-43. Genomic DNA was collected from
421 each fraction using the NucleoSpin Blood Kit (Macherey Nagel 740950.50) following
422 manufacturer's instructions. Briefly, cells were washed in PBS and resuspended in PBS
423 containing proteinase K. Next BQ1 was added to each tube and mixed by vortexing. Samples
424 were incubated at 56˚C for 15 minutes and cooled to room temperature for at least 30 minutes.
425 100% ethanol was added to the tube and mixed by vortexing before loading onto the column.
426 Columns were spun for 3 minutes at 4000 xg and flow through discarded. BQ2 was added to
427 the column and columns spun for 2 minutes at 4000 xg. BQ2 step was repeated a total of 2
428 times. To elute genomic DNA, pre-heated BE was added to each column, incubated for 5
429 minutes at room temperature, and spun for 4 minutes at 4000 xg in a new tube. Elution was
430 repeated a second time. Next, sgRNA amplicons were enriched using primers containing
431 indexing barcodes and Illumina adapters. 10 µg of genomic DNA was used per PCR reaction.
432 PCR reactions also contained 100 µM of one of the following indexed forward primer
433 (caagcagaagacggcatacgagatcgctcagttctgctatgctgtttccagcttagctcttaaac,
434 caagcagaagacggcatacgagattatctgaccttgctatgctgtttccagcttagctcttaaac,
435 caagcagaagacggcatacgagatatatgagacgtgctatgctgtttccagcttagctcttaaac,
436 caagcagaagacggcatacgagatcttatggaattgctatgctgtttccagcttagctcttaaac), 100 µM of one of the
437 following indexed reverse primer
438 (aatgatacggcgaccaccgagatctacactcgtggagcgagcacaaaaggaaactcaccctaactgt,
439 aatgatacggcgaccaccgagatctacacctacaagataagcacaaaaggaaactcaccctaactgt,
440 aatgatacggcgaccaccgagatctacactatagtagctagcacaaaaggaaactcaccctaactgt,
441 aatgatacggcgaccaccgagatctacactgcctggtggagcacaaaaggaaactcaccctaactgt) and 1x NEBNext
442 Ultra Q5 MasterMix (NEB M0544L). Cycling parameters were as follows: 98˚C for 30 seconds,
443 22-24 cycles of 98˚C for 10 seconds, 66˚C for 75 seconds, then a 5-minute hold at 72˚C after
444 cycles and a hold at 4˚C. PCR reactions were pooled and leaned up with a PCR purification. A
445 0.5X-0.65X SPRI cleanup as performed prior to sequencing. Half volume of SPRI beads
446 (Beckman Coulter B23318) were added to the pooled PCR reaction and incubated at room
447 temperature for 10 minutes. Beads were removed with a magnet and supernatant collected.
448 Next, a 0.65 volume of SPRI beads were added to cleared supernatant, incubated at room
449 temperature for 10 minutes and tubes placed on a magnetic stand. Supernatant was removed
450 and discarded. Beads were washed with fresh 80% ethanol twice and beads air dried for 2-5
451 minutes. Sample was eluted in 30 µL EB buffer. The SRPI PCR cleanup was repeated in its
452 entirety to remove excess primer contamination. PCR product yield, size, and quality was
453 checked on a Bioanalyzer (Agilent) with a High Sensitivity DNA chip (Agilent B23318). Enriched
454 PCR product is 562 base pairs in length. Samples were sequenced on the MiSeq with 1% PhiX
455 through paired end 50 sequencing with custom primers (Read1:
456 gtgtgttttgagactataagtatcccttggagaaccaccttgttgg, Read2: tgctatgctgtttccagcttagctcttaaac, i7

457 Indexing primer: aagagctaagctggaaacagcatagca). Sequencing files were demultiplexed based
458 on the sample PCR. To remove recombined dual guides, fastq files were filtered for reads
459 containing paired guides for the same target gene using the parser.py file
460 (https://github.com/NIH-CARD). The parsed dual hits file was analyzed using the standard
461 MAGeCKFlute robust ranked algorithm (RRA) pipeline[50] comparing the high 25% to low 25% of
462 the TDP-43 HaloTag fluorescence (results in Tables S1-4). The RRA uses a negative binomial
463 model to generate p-values to rank guides from negative to positive. Guide output files were
464 filtered to remove low count guides and used to generate rank plots of target guides and non-
465 targeting negative controls. All data and code for plots is available on
466 (https://github.com/jhawrot/TDP_BORC/tree/main).
467
468 *CRISPRi meta-analysis*
469 CRISPRi FACS screens in i^{3}Neurons[11] were obtained from CRISPRBrain
470 (https://crisprbrain.org/) and the Kampmann lab and underwent data harmonization with the
471 screens presented here. First, screen phenotype scores and log fold changes were aligned by
472 converting effect estimates to standardized beta values represented by z-scores. Next, extreme
473 p-values were stabilized by truncation to prevent distortions in the statistical tests due to outliers
474 or very small probabilities, ensuring a robust meta-analysis, accommodating the floating point of
475 the system and acknowledging that this truncation will cause results to be more conservative.
476 Standard errors of the effect estimates were derived by dividing the beta estimate by the
477 absolute value of the z-scores. Fixed effect meta-analyses were then carried out for all possible
478 screen combinations (combining already published versus novel screens). These functions
479 calculate pooled estimates of effect sizes, variance, and test for heterogeneity among screens.
480 Novelty was assessed by filtering associations that were not significant after multiple test
481 corrections in either of the constituent datasets but were significant after false-discovery rate
482 adjustment of the meta-analysis. Data was visualized using modified MAGeCKFlute pipelines to
483 assess putative biological functions of significant genes using published enrichment functions
484 including clusterProfiler, GOstats, enrich.HGT, and GSEA packages. TDP-43 expression hits
485 were grouped into positive and negative modifiers using Log2FC values, and statistical
486 significance was assessed by gene ratio or FDR depending on the enrichment analysis. Code is
487 available on (https://github.com/NIH-CARD/V_Ryan_TDP43_meta_2024).
488
489 *Lentivirus production and transduction*
490 Individual CRISPRi knockdowns were performed by cloning sgRNAs into pU6-sgRNA
491 EF1Alpha-puro-T2A-BFP (Addgene plasmid # 60955). sgRNA sequences for screen validation
492 are listed in Table S5. To make lentivirus, Lenti-X human embryonic kidney (HEK) cells were
493 split with trypsin, plated on poly-L-ornithine coated plates, and allowed to recover. Cells were
494 then transfected with sgRNA plasmids on a 6 well plate using 3.75 µL Lipofectamine 3000
495 Reagent and 5 µL P3000 Enhancer Reagent (Invitrogen, L3000075), Opti-MEM (Gibco,
496 31985062), psPAX2 F46, pMD2G F45, and pAdVantage F44. Transfected cells were cultured
497 for two days in DMEM supplemented with GlutaMAX--I (Thermo Fisher Scientific, 35050061)
498 and 10% Fetal Bovine Serum (FBS) (Sigma-Aldrich, F4135). Media was then changed and
499 supplemented with (1:500) viral boost reagent (ALSTEM, VB100), and cells were cultured for
500 two days before media was harvested and Lenti-X Concentrator (Takara Bio USA, 631231) was
501 added at (1:3) to concentrate the virus for 2-3 days at 4°C. Virus was then collected, aliquoted,
502 and stored at -80°C until use.
503 iPSCs were transduced at scales of 0.1-1e6 cells per 100 µL concentrated virus while
504 cells were in suspension. Cells were allowed to recover for two days before 10 µg/mL
505 puromycin dihydrochloride (Sigma-Aldrich, P9620) was added for selection. For cells that were
506 differentiated, transduction was performed four days before initiating neuronal differentiation.
507

508 *Validation of hits from genome wide screens*
509 Hits from the screen were validated by microscopy with individual sgRNA knockdowns in
510 i11w-hT neurons. Cells were plated, transduced, and differentiated as described above.
511 Fluorescent HaloTag ligand JF646 (Promega, GA112A) was added at 200 µg/mL approximately
512 15 minutes before microscopy. Cells were imaged on Nikon Ti2 with automated stage at 20x
513 with exposure times of 100ms for all channels. Laser power was as follows: 640 nm at 100%,
514 405 nm at 25%, and 561 nm at 100%. Halo-TDP-43 fluorescent intensity was quantified using
515 CellProfiler[51] or Nikon Elements General Analysis 3 and graphed in GraphPad Prism.
516 sgRNAs for genes selected for further validation on untagged TDP-43 were transduced
517 into i11w-mNC iPSCs and neurons differentiated as above. On day 7, neurons were fixed with
518 4% PFA (Thermo Fisher Scientific, 28906) for 10 minutes at room temperature. PFA was
519 removed and cells washed in PBS. Cells were then permeabilized with 0.1% Triton-X 100
520 (Sigma-Aldrich, 93443) for 10 minutes before blocking in 2% bovine serum albumin (BSA)
521 (Jackson ImmunoResearch, 001-000-162) for 10 minutes. TDP-43 primary antibody
522 (Proteintech, 10782-2-AP) was diluted 1:1000 in 2% BSA and added to cells at 4˚C overnight.
523 After washing, Donkey Anti-Rabbit IgG (H+L), Highly Cross-Adsorbed secondary antibody
524 (CF488, Biotium, 20015) was added at 1:1000 in 2% BSA for 1 hour at room temperature. Cells
525 were washed and DRAQ5 nuclear stain (Thermo Fisher Scientific, 62251) was added at 1:1000
526 dilution in PBS for 5 minutes. DRAQ5 was washed out with PBS three times before imaging.
527 Stained cells were imaged on Nikon Ti2 with automated stage at 20x and an exposure time of
528 100 ms for 640nm and 488nm and 200 ms for 405nm. Laser power was 100% for all channels.
529 TDP-43 fluoresce intensity was quantified using Nikon Elements and graphed in GraphPad
530 Prism.
531
532 *Lysosome drug treatment*
533 i11w-hT iPSCs were cultured and differentiated into neurons. i11w-mNC, treated for 24
534 hours with DMSO, were used as a Halo-negative control. Microscopy was performed on day 7
535 of neuronal differentiation. Wells were individually treated with drugs by removing half the media
536 and adding back an equal volume of media containing 2x final concentration of each drug, for
537 timepoints as stated below. A volume of DMSO equal to the largest volume of drug was added
538 at the earliest timepoint to wells as a negative control for treatment. Treatments were as follows:
539 50 µM Chloroquine (Selleck Chemicals, S6999) for 24 hours; 50 µM CA-074me (Selleck
540 Chemicals, S7420), a Cathepsin B Inhibitor (CTSBI), for 6 hours; 30 mM Ammonium Chloride
541 (NH_4Cl) (Sigma-Aldrich, A9434) for 5 hours; 500 nM Bafilomycin A1 (BafA1) (LKT Labs, B0025)
542 for 4 hours; 1x Lysosome Protease Inhibitor Cocktail (20 µM E64 (Selleck Chemicals, S7379),
543 10 µM pepstatin A (Selleck Chemicals, S7381) and 50 µM leupeptin (Sigma-Aldrich, L2884);
544 referred to in Figure S5B-C as Protease Inhibitor) for 4 hours; 1 mM L-Leucyl-L-Leucine methyl
545 ester (hydrochloride) (LLOME) (Cayman Chemical Company, 16008) for 4 hours; 400 µM Gly-
546 Phe-β-naphthylamide (GPN) (Cayman Chemical Company, 14634) for 1 hour; 500 µM Sodium
547 (meta) arsenite (NaAsO2) (Sigma-Aldrich, S7400), 1 hours; 40 µM Anisomycin (Sigma-Aldrich,
548 A5862) for 1 hour; and 0.1 mg/mL Cycloheximide solution (CHX) (Sigma-Aldrich, C4859) for 45
549 minutes. Fluorescent HaloTag ligand was added as described above 15 minutes prior to
550 imaging. Cells were imaged on Nikon Ti2 with automated stage at 20x in 640nm with an
551 exposure time of 100ms and 100% laser power. Halo-TDP-43 fluorescent intensity was
552 quantified using Nikon Elements and graphed in GraphPad Prism.
553
554 *Live cell imaging of TDP-43 motion and organelle co-localization*
555 i11w-hT iPSCs were transduced with fluorescent tags for mitochondrial targeted
556 mEmerald and LAMP1 tagged with mApple. The cells were then transduced with either

557 BORCS6 or BORCS7 knockdown and non-targeting control guides. BORCS6 knockdown cells
558 were cultured and differentiated as described above. BORCS7 knockdown cells were
559 differentiated as neurospheres. Fluorescent HaloTag ligand was added to day 7 BORCS6
560 knockdown neurons and day 10 BORCS7 knockdown neurospheres, as described above. Cells
561 were imaged on Nikon Ti2 with automated stage at 60x and exposure times of 100 ms for all
562 channels. Laser power was 100% for 640nm and 561nm. 405nm and 488nm lasers were set at
563 100% and 99.4%, respectively, for BORCS6 knockdown cells, and at 50% for BORCS7
564 knockdown neurospheres. DAPI image was taken once at the beginning of the video; GFP,
565 Cy5, and RFP channels were captured over 30 seconds with no delay between frames and an
566 approximate frames per second (FPS) of 1.16. Puncta were counted from kymographs of
567 axonal segments made in ImageJ or Nikon Elements and graphed in GraphPad Prism.
568
569 *qPCR*
570 qPCR was performed using TaqMan Real-Time PCR assays. RNA was extracted from
571 BORC and TDP-43 knockdown and non-targeting control i11-mNC-derived neurons using the
572 RNeasy Plus Mini kit (QIAGEN, 74134). RNA concentrations were measured with a DeNovix
573 DS-11 FX+ 1uL Spectrophotometer, and 855 ng of RNA was used as input for reverse
574 transcription. Reverse transcription was performed using the High-Capacity cDNA Reverse
575 Transcription Kit (Thermo Fisher Scientific, 4368814). The qPCR reaction was performed with
576 2x TaqMan Universal PCR Master Mix (Thermo Fisher Scientific, 4304437) on an Applied
577 Biosystems QuantStudio 6 Flex Real-Time PCR System. Probes were run singleplex. The
578 Taqman probe for the target was TARDBP, (FAM-MGB Hs00606522_m1, Thermo Fisher
579 Scientific, 4453320). Two endogenous controls were used: PPIA (VIC-MGB-PL
580 Hs04194521_s1, Thermo Fisher Scientific, 4448484); and PGK1, TaqMan ID: Hs00943178_g1,
581 VIC-MGB-PL, (Thermo Fisher Scientific, 4448484). Relative change in gene expression was
582 examined using the 2^-(ΔΔCt) analysis method[52]. Significance was evaluated using an ordinary
583 one-way ANOVA with the Šidák correction for multiple comparisons.
584
585 *pLentiCRISPR*
586 A non-targeting (AGAGTTACGTCGCTTCGATC) and two sgRNA targeting sequences
587 against BORCS7 (1: CGCGATTACGTCAGTACCAC, 2: GATTACGTCAGTACCACAGG) were
588 cloned into the lenti-CRISPR v2 plasmid (Addgene 52961) following the Zhang Lab protocol
589 (https://media.addgene.org/data/plasmids/52/52961/52961-attachment_B3xTwla0bkYD.pdf).
590 Briefly, the plasmid was digested with BsmBI-v2 (NEB R0739), the cut vector was
591 dephosphorylated with NEB Quick CIP (NEB M0525), and digested and dephosphorylated
592 vector was extracted from an agarose gel. Primers containing the sgRNA targeting sequences
593 (Eurofins) were phosphorylated with T4 PNK (NEB M0201) and annealed before being ligated
594 into the cut vector using 2x Ligation Master Mix (Takara 6023). After sequencing to confirm
595 correct cloning, plasmids were transfected into Lenti-X HEK cells using standard protocols (see
596 above). Virus was then transduced into i11w-mN iPSCs and selected with puromycin using
597 standard protocols (see above). Selected iPSCs were differentiated using standard protocols
598 (see above). On day 7 post dox induction, neurons were fixed and immunofluorescence
599 performed as above.
600
601 *SunTag TDP-43 translation assay*
602 TDP-43 coding sequence and 3'UTR were cloned into a plasmid expressing 24 SunTag
603 repeats under an Ef1alpha promoter followed by 24 PP7 stem loops[36] (modified from Addgene
604 74928). This plasmid was transfected into iPSCs stably expressing the SunTag scFv tagged
605 with HaloTag under an Ef1alpha promoter (modified from Addgene 60907), PP7 coat protein
606 tagged to 3 SnapTags (synthesized), and mEmerald-tagged lysosomes (to validate BORC KD).

607 iPSCs were transduced with sgRNA and differentiated as spheres before plating on an 8 well
608 glass bottom µ-Slide (Ibidi, 80827). Neurospheres were imaged at d10 post dox induction on a
609 Nikon Ti2 spinning disk confocal microscope at 60x with only neurites in the field of view.
610 Exposure times were as follows: 300 ms for 640nm, 200 ms for 561, 200 ms for 488, and
611 100ms for 405. Laser power was at 50% for DAPI and 100% for all other channels. Images
612 were quantified for co-localized PP7 and SunTag (SnapTag and HaloTag, respectively) puncta
613 using Nikon Elements. Resulting data were graphed in GraphPad Prism.
614
615 *RNA sequencing*
616 RNA was extracted from day 7 BORCS6 knockdown and non-targeting control i11-mNC
617 neurons using the Direct-zol-96 MagBead RNA kit (Zymo Research, R2103). Manufacturer
618 protocol was followed, including the optional DNAase step, with volumes increased for an
619 automated run on the KingFisher. Quantified with Qbit and frozen at -80°C. RNA quality was
620 checked on a BioAnalyzer and Strand-Specific RNA-seq library preparation was performed with
621 rRNA depletion using the NEBNext® Ultra™ II Directional RNA Library Prep Kit for Illumina®
622 (New England Biolabs, E7760) and the NEBNext® Globin & rRNA Depletion Kit. (New England
623 Biolabs, E7750). Samples were run on an Illumina NovaSeq X 10B on a 2 x 150 bp flow cell.
624
625 *Bulk RNA sequencing analysis*
626 Gene length normalized counts per gene were generated and then within sample
627 normalization using counts per million (cpm) was performed. Next, pedestalling using a value of
628 2 and log2 transformation were performed. Cyclicloess was used to normalize expression
629 across samples followed by exploratory analysis to insepct for and remove outlier samples if
630 present. If present, cyclicloess nomrlaization is repeated. Data post cyclicloess normalization is
631 then noise modeled (CV~mean) by experiment condition (NT v KD) and a noise threshold for
632 the data defined. This noise threshold is then used to filter remove noise-biased genes with
633 surviving genes then subject to differential testing using the appropriate test. After differential
634 testing, all statistics are captured and exported along with confirmatory visual generation post
635 differential gene selection. Pathway analysis was performed to identify enriched pathways and
636 functions for each comparison performed as part of differential testing. Alternative poly
637 adenylation was assessed using REPAC[35]. Results that had an absolute compositional Fold
638 Change (cFC) >= 0.25 and an FDR corrected p-value < 0.05 were considered Poly Adenylation
639 Sites that had a significant shortening (negative cFC) or lengthening event (positive cFC) and
640 were plotted using VolcaNoseR[53]. GO analysis of alternative poly-adenylation was performed
641 using ShinyGO[54].
642
643 *Cryptic splicing analysis*
644 For cryptic splicing analyses, sequencing files were aligned to GRCh38 reference
645 genome (STAR v2.7.3a)[55]. We ran MAJIQ (v2.1)[56] on aligned BAM files using a custom
646 Snakemake (v 5.5.4)[57] pipeline (https://github.com/frattalab/splicing). A threshold of 10%
647 difference in percent spliced in (PSI, ΔΨ) was used to identify a significant change between
648 groups. We defined cryptic splicing as junctions with ΔΨ > 10% that were present in <5% of
649 control samples or ΔΨ < -10% that were present in >10% of control samples. An additional
650 pipeline developed previously[34] was used to visualize and categorize each mis-spliced junction
651 as cryptic exon, exon skipping, intron retention, or canonical junction (https://github.com/NIH-
652 CARD/proteogenomic-pipeline).
653
654 *Proteomic sample preparation*
655 BORC knockdown and non-targeting control i11w-mNC cells were cultured and
656 differentiated as described above until day 5 of neuronal differentiation. On day 5, half of the
657 cultures were changed to heavy-SILAC media ("dSILAC samples"), which was DMEM for SILAC

658 (Thermo Fisher Scientific, 88364) supplemented with B27 Plus Supplement (Thermo Fisher
659 Scientific, A3582801), 10 ng/mL BDNF (PeproTech, 450-02), 10 ng/mL NT-3 (PeproTech, 450-
660 03), 1 µg/mL mouse laminin (Sigma, L2020-1MG), 50 nM Chroman-1 (MedChemExpress
661 Catalog #HY-15392), 2 µg/mL doxycycline (Clontech, 631311), 0.5 mM lysine, and 0.3 mM
662 arginine. Heavy SILAC media was supplemented with L-Lysine:2HCl (13C6, 99%; 15N2, 99%)
663 (Cambridge Isotope Laboratories, Inc., CNLM-291-H) and L-Arginine:HCl (13C6, 99%; 15N4,
664 99%) (Cambridge Isotope Laboratories, Inc., CNLM-539-H). Remaining cultures were
665 maintained in light SILAC media made with L-Lysine monohydrochloride (SIGMA, L8662 and
666 L7039) and L-Arginine monohydrochloride (SIGMA, A4599) to produce non-SILAC samples to
667 evaluate changes in total protein abundance. Half-media changes were performed every other
668 day or every 3 days. Cells were harvested on day 7 and day 15 post-dox induction.
669 Protein was extracted from day 7 and day 15 neurons for mass spectrometry as done
670 previously[58]. Neurons were gently washed with PBS, then SP3 lysis buffer (50 mM Tris-HCl
671 (Thermo Fisher Scientific, 15568025), 50 mM NaCl (Thermo Fisher Scientific, 24740011), 1%
672 SDS (Thermo Fisher Scientific, 15553027), 1% Triton X-100 (MilliporeSigma, X100), 1% NP-40
673 (Thermo Fisher Scientific, 85124), 1% Tween 20 (MilliporeSigma, P9416), 1% glycerol (MP
674 Biomedicals, 800687), 1% Sodium deoxycholate (wt/vol) (MilliporeSigma D6750), 5 mM EDTA,
675 5mM Dithiothreitol (DTT) (Thermo Fisher Scientific, R0862), 5 KU Benzonase (Sigma-Aldrich,
676 E8263), and 1× cOmplete ULTRA Protease Inhibitor Tablets (one tablet per 10mL of lysis
677 buffer) (Sigma-Aldrich, 5892791001)) was added directly to the wells. Neurons were scraped
678 into the buffer to aid with lysis. Proteins were alkylated with 10 mM Iodoacetamide (IAA)
679 (Thermo FIsher Scientific, A39271) at room temperature in the dark, then reduced by adding 2
680 µL of 500 mM DTT to the lysate and incubating at 25˚C for 30 min in the light. A Thermo Fisher
681 KingFisher Apex was used to perform the automated SP3 protein enrichment protocol. This
682 protocol uses SP3 beads: GE SpeedBeads (GE45152105050250) and of GE SpeedBeads
683 (GE65152105050250) combined in a 1:1 ratio. The SP3 beads are washed in LC-MS grade
684 water (Pierce, 51140) and reconstituted in 50% EtOH at a concentration of 4 mg/mL. Samples
685 are diluted 1:1 with 100% EtOH, washed in 80% EtOH, and eluted in 50 mM ammonium
686 bicarbonate with 20 µg/mL lyophilized trypsin/LysC (Promega, V5073). After completion of the
687 KingFisher SP3 protocol, samples were shaken overnight at 37˚C. The KingFisher was used to
688 perform a bead removal protocol twice. Solvents were removed in a speed vac. Samples were
689 stored dry at -20˚C until resuspension in 2% acetonitrile (Thermo Fisher Scientific, 51101), 0.4%
690 Trifluoroacetic acid (TFA) (Thermo Fisher Scientific, 85183), and 0.1% formic acid (Thermo
691 Fisher Scientific, 28905).
692
693 *LC-MS analysis*
694 Peptide concentration from each sample was measured on a DeNovix DS-11 FX+ 1uL
695 Spectrophotometer and normalized to 0.5 µg/µL. LC-MS/MS experiments were performed on a
696 Thermo Scientific Orbitrap Lumos Tribrid Mass Spectrometer couple with a Thermo Scientific
697 Ultimate 3000 HPLC system. The injection volume for each sample was 2 µl. Peptides were
698 separated on a Thermo Scientific ES902 column (particle Size: 2 µm, diameter: 75 µm, length:
699 25 cm). Mobile phase A contains 0.1% formic acid in LC-MS grade water, and Mobile phase B
700 contains 0.1% formic acid in LC-MS grade acetonitrile. Mobile phase B was increased from 3%
701 to 22% in 64 min, then from 22% to 36% in 8 min. LC-MS/MS data were acquired in data-
702 dependent mode. The MS1 scans were performed in orbitrap with a resolution of 120K, a mass
703 range of 375-1500 m/z, and an AGC target of 4 x 105. The quadrupole isolation window is 1.6
704 m/z. The precursor ion intensity threshold to trigger the MS/MS scan was set at 1 x 104. MS2
705 scans were conducted in the ion trap. Peptides were fragmented with the HCD method and the

collision energy was set at 30%. The maximum ion injection time was 35 ms. MS1 scan was performed every 3 sec. As many MS2 scans were acquired within the 3-sec cycle.

Proteomic data analysis

Proteomic raw data were analyzed using MaxQuant software (v. 1.6.14)[59]. A reviewed Swiss-Prot *Homo sapiens* database and a custom neuron-specific contaminant FASTA library[60] (available to download at https://github.com/HaoGroup-ProtContLib) were used for protein and peptide identifications with a 1% false discovery rate cutoff. A maximum of two missed cleavages were allowed. A maximum of three variable modifications were allowed for cysteine N-ethylmaleimide, methionine oxidation, and protein N-terminus acetylation. Precursor and fragment tolerances were set to 25 ppm. Contaminatn proteins and peptides were removed. Protein intensities from protein.txt output files were used for nonSILAC data analysis. dSILAC data was analyzed using a previously established workflow[61]. A standard multiplicity with two labels was enabled for SILAC data, and Lys8/Arg10 was selected as the heavy channel. For SILAC proteomics, only y-type product ions with up to two charges were used for quantification. The "peptide.txt" report was exported for subsequent analysis in R. Peptides from contaminant proteins and peptides with intensities below 1000 were removed. Peptides with heavy/light ratios lower than 0.01 or higher than 100 were also removed to avoid outlier half-life measurements. A single timepoint calculation was used to calculate peptide half-lives assuming a steady state of turnover: $t_{1/2} = t_s \times \frac{ln\,(2)}{ln\,(1+R)}$, where R is the heavy-to-light ratio and ts is the labeling time point after media switch as described previously[61]. Protein half-lives were then determined as the harmonic mean of half-lives from unique peptides belonging to each protein.

Phosphopeptides were identified in cells cultured exclusively in light media. We employed the FragPipe LFQ-phospho workflow to detect and quantify modified peptides from our spectral files. This workflow integrates MSFragger for peptide identification with match-between-runs enabled[62], PTMProphet for precise mass modification localization[63], and Philosopher for false discovery rate filtering and reporting[64]. Differential expression of phosphopeptides was subsequently assessed in R (version 4.4.3) using the limma package (version 3.62.2). A threshold of a 1 log-fold change combined with a Benjamini-Hochberg adjusted p-value of 0.05 was applied to define significantly differentially expressed phosphosites.

Data Availability

RNA sequencing data files can be accessed at GEO Accession Number GSE299976 and the Alzheimer's Disease Workbench (ADWB https://fair.addi.ad-datainitiative.org/#/data/datasets/borcs6_kd_transcriptomics_on_ineurons). The mass spectrometry proteomics data have been deposited to the ProteomeXchange Consortium via the PRIDE partner repository with the dataset identifier PXD063206[65].

Acknowledgements

We thank Sami Barmada, Derek Narendra, and Achim Werner for their insights into the best genes from the screens to follow up on within their subject matter expertise. We thank the NIH Intramural Sequencing Center for performing RNA sequencing, the Sequencing Cores at the National Heart, Lung, and Blood Institute for sequencing screen samples, and the Proteomics Core at the National Institute of Neurological Disorders and Stroke for performing mass spec. This work was supported by the National Institute of Neurological Disorders and Stroke and the Center for Alzheimer's and Related Dementias, within the Intramural Research Program of the National Institute on Aging, National Institutes of Health, Department of Health and Human Services. M.E.W. was additionally supported by funding through the Chan Zuckerberg Initiative. V.H.R. was supported in part by the National Institute of General Medical Sciences

Fi2GM142475. L.H. was supported in part by the National Institute of Neurological Disorders and Stroke R01NS121608.

References

1. Meneses A, Koga S, O'Leary J, Dickson DW, Bu G, Zhao N. TDP-43 Pathology in Alzheimer's Disease. Mol Neurodegener. 2021;16(1):84. Epub 20211220. doi: 10.1186/s13024-021-00503-x. PubMed PMID: 34930382; PMCID: PMC8691026.
2. Tziortzouda P, Van Den Bosch L, Hirth F. Triad of TDP43 control in neurodegeneration: autoregulation, localization and aggregation. Nat Rev Neurosci. 2021;22(4):197-208. Epub 20210302. doi: 10.1038/s41583-021-00431-1. PubMed PMID: 33654312.
3. Baughn MW, Melamed Z, Lopez-Erauskin J, Beccari MS, Ling K, Zuberi A, Presa M, Gonzalo-Gil E, Maimon R, Vazquez-Sanchez S, Chaturvedi S, Bravo-Hernandez M, Taupin V, Moore S, Artates JW, Acks E, Ndayambaje IS, Agra de Almeida Quadros AR, Jafar-Nejad P, Rigo F, Bennett CF, Lutz C, Lagier-Tourenne C, Cleveland DW. Mechanism of STMN2 cryptic splice-polyadenylation and its correction for TDP-43 proteinopathies. Science. 2023;379(6637):1140-9. Epub 20230316. doi: 10.1126/science.abq5622. PubMed PMID: 36927019; PMCID: PMC10148063.
4. Arnold ES, Ling SC, Huelga SC, Lagier-Tourenne C, Polymenidou M, Ditsworth D, Kordasiewicz HB, McAlonis-Downes M, Platoshyn O, Parone PA, Da Cruz S, Clutario KM, Swing D, Tessarollo L, Marsala M, Shaw CE, Yeo GW, Cleveland DW. ALS-linked TDP-43 mutations produce aberrant RNA splicing and adult-onset motor neuron disease without aggregation or loss of nuclear TDP-43. Proc Natl Acad Sci U S A. 2013;110(8):E736-45. Epub 20130204. doi: 10.1073/pnas.1222809110. PubMed PMID: 23382207; PMCID: PMC3581922.
5. Highley JR, Kirby J, Jansweijer JA, Webb PS, Hewamadduma CA, Heath PR, Higginbottom A, Raman R, Ferraiuolo L, Cooper-Knock J, McDermott CJ, Wharton SB, Shaw PJ, Ince PG. Loss of nuclear TDP-43 in amyotrophic lateral sclerosis (ALS) causes altered expression of splicing machinery and widespread dysregulation of RNA splicing in motor neurones. Neuropathol Appl Neurobiol. 2014;40(6):670-85. doi: 10.1111/nan.12148. PubMed PMID: 24750229.
6. Ling SC, Polymenidou M, Cleveland DW. Converging mechanisms in ALS and FTD: disrupted RNA and protein homeostasis. Neuron. 2013;79(3):416-38. doi: 10.1016/j.neuron.2013.07.033. PubMed PMID: 23931993; PMCID: PMC4411085.
7. Mackenzie IR, Neumann M. Reappraisal of TDP-43 pathology in FTLD-U subtypes. Acta Neuropathol. 2017;134(1):79-96. Epub 20170502. doi: 10.1007/s00401-017-1716-8. PubMed PMID: 28466142.
8. Nana AL, Sidhu M, Gaus SE, Hwang JL, Li L, Park Y, Kim EJ, Pasquini L, Allen IE, Rankin KP, Toller G, Kramer JH, Geschwind DH, Coppola G, Huang EJ, Grinberg LT, Miller BL, Seeley WW. Neurons selectively targeted in frontotemporal dementia reveal early stage TDP-43 pathobiology. Acta Neuropathol. 2019;137(1):27-46. Epub 20181203. doi: 10.1007/s00401-018-1942-8. PubMed PMID: 30511086; PMCID: PMC6339592.
9. Doench JG. Am I ready for CRISPR? A user's guide to genetic screens. Nat Rev Genet. 2018;19(2):67-80. Epub 20171204. doi: 10.1038/nrg.2017.97. PubMed PMID: 29199283.
10. Tian R, Gachechiladze MA, Ludwig CH, Laurie MT, Hong JY, Nathaniel D, Prabhu AV, Fernandopulle MS, Patel R, Abshari M, Ward ME, Kampmann M. CRISPR Interference-Based Platform for Multimodal Genetic Screens in Human iPSC-Derived Neurons. Neuron. 2019;104(2):239-55 e12. Epub 20190815. doi: 10.1016/j.neuron.2019.07.014. PubMed PMID: 31422865; PMCID: PMC6813890.
11. Tian R, Abarientos A, Hong J, Hashemi SH, Yan R, Drager N, Leng K, Nalls MA, Singleton AB, Xu K, Faghri F, Kampmann M. Genome-wide CRISPRi/a screens in human neurons link lysosomal failure to ferroptosis. Nat Neurosci. 2021;24(7):1020-34. Epub

806 20210524. doi: 10.1038/s41593-021-00862-0. PubMed PMID: 34031600; PMCID:
807 PMC8254803.
808 12. Replogle JM, Bonnar JL, Pogson AN, Liem CR, Maier NK, Ding Y, Russell BJ, Wang X,
809 Leng K, Guna A, Norman TM, Pak RA, Ramos DM, Ward ME, Gilbert LA, Kampmann M,
810 Weissman JS, Jost M. Maximizing CRISPRi efficacy and accessibility with dual-sgRNA libraries
811 and optimal effectors. Elife. 2022;11. Epub 20221228. doi: 10.7554/eLife.81856. PubMed PMID:
812 36576240; PMCID: PMC9829409.
813 13. Pu J, Schindler C, Jia R, Jarnik M, Backlund P, Bonifacino JS. BORC, a multisubunit
814 complex that regulates lysosome positioning. Dev Cell. 2015;33(2):176-88. doi:
815 10.1016/j.devcel.2015.02.011. PubMed PMID: 25898167; PMCID: PMC4788105.
816 14. Avendano-Vazquez SE, Dhir A, Bembich S, Buratti E, Proudfoot N, Baralle FE.
817 Autoregulation of TDP-43 mRNA levels involves interplay between transcription, splicing, and
818 alternative polyA site selection. Genes Dev. 2012;26(15):1679-84. doi:
819 10.1101/gad.194829.112. PubMed PMID: 22855830; PMCID: PMC3418585.
820 15. Samelson AJ, Ariqat N, McKetney J, Rohanitazangi G, Bravo CP, Bose R, Travaglini KJ,
821 Lam VL, Goodness D, Dixon G, Marzette E, Jin J, Tian R, Tse E, Abskharon R, Pan H, Carroll
822 EC, Lawrence RE, Gestwicki JE, Eisenberg D, Kanaan NM, Southworth DR, Gross JD, Gan L,
823 Swaney DL, Kampmann M. CRISPR screens in iPSC-derived neurons reveal principles of tau
824 proteostasis. bioRxiv. 2024. Epub 20241104. doi: 10.1101/2023.06.16.545386. PubMed PMID:
825 37398204; PMCID: PMC10312804.
826 16. Replogle JM, Saunders RA, Pogson AN, Hussmann JA, Lenail A, Guna A, Mascibroda
827 L, Wagner EJ, Adelman K, Lithwick-Yanai G, Iremadze N, Oberstrass F, Lipson D, Bonnar JL,
828 Jost M, Norman TM, Weissman JS. Mapping information-rich genotype-phenotype landscapes
829 with genome-scale Perturb-seq. Cell. 2022;185(14):2559-75 e28. Epub 20220609. doi:
830 10.1016/j.cell.2022.05.013. PubMed PMID: 35688146; PMCID: PMC9380471.
831 17. Sanjana NE, Shalem O, Zhang F. Improved vectors and genome-wide libraries for
832 CRISPR screening. Nat Methods. 2014;11(8):783-4. doi: 10.1038/nmeth.3047. PubMed PMID:
833 25075903; PMCID: PMC4486245.
834 18. Root J, Merino P, Nuckols A, Johnson M, Kukar T. Lysosome dysfunction as a cause of
835 neurodegenerative diseases: Lessons from frontotemporal dementia and amyotrophic lateral
836 sclerosis. Neurobiol Dis. 2021;154:105360. Epub 20210331. doi: 10.1016/j.nbd.2021.105360.
837 PubMed PMID: 33812000; PMCID: PMC8113138.
838 19. Rhinn H, Tatton N, McCaughey S, Kurnellas M, Rosenthal A. Progranulin as a
839 therapeutic target in neurodegenerative diseases. Trends Pharmacol Sci. 2022;43(8):641-52.
840 Epub 20220115. doi: 10.1016/j.tips.2021.11.015. PubMed PMID: 35039149.
841 20. Hung C, Patani R. 4R tau drives endolysosomal and autophagy dysfunction in
842 frontotemporal dementia. Autophagy. 2024;20(5):1201-2. Epub 20240109. doi:
843 10.1080/15548627.2023.2300917. PubMed PMID: 38174587; PMCID: PMC11135858.
844 21. Wallings RL, Humble SW, Ward ME, Wade-Martins R. Lysosomal Dysfunction at the
845 Centre of Parkinson's Disease and Frontotemporal Dementia/Amyotrophic Lateral Sclerosis.
846 Trends Neurosci. 2019;42(12):899-912. Epub 20191105. doi: 10.1016/j.tins.2019.10.002.
847 PubMed PMID: 31704179; PMCID: PMC6931156.
848 22. Talaia G, Bentley-DeSousa A, Ferguson SM. Lysosomal TBK1 responds to amino acid
849 availability to relieve Rab7-dependent mTORC1 inhibition. EMBO J. 2024. Epub 20240805. doi:
850 10.1038/s44318-024-00180-8. PubMed PMID: 39103493.
851 23. Ling SC, Dastidar SG, Tokunaga S, Ho WY, Lim K, Ilieva H, Parone PA, Tyan SH, Tse
852 TM, Chang JC, Platoshyn O, Bui NB, Bui A, Vetto A, Sun S, McAlonis-Downes M, Han JS,
853 Swing D, Kapeli K, Yeo GW, Tessarollo L, Marsala M, Shaw CE, Tucker-Kellogg G, La Spada
854 AR, Lagier-Tourenne C, Da Cruz S, Cleveland DW. Overriding FUS autoregulation in mice
855 triggers gain-of-toxic dysfunctions in RNA metabolism and autophagy-lysosome axis. Elife.

2019;8. Epub 20190212. doi: 10.7554/eLife.40811. PubMed PMID: 30747709; PMCID: PMC6389288.
24. Beckers J, Tharkeshwar AK, Van Damme P. C9orf72 ALS-FTD: recent evidence for dysregulation of the autophagy-lysosome pathway at multiple levels. Autophagy. 2021;17(11):3306-22. Epub 20210226. doi: 10.1080/15548627.2021.1872189. PubMed PMID: 33632058; PMCID: PMC8632097.
25. Ormeno F, Hormazabal J, Moreno J, Riquelme F, Rios J, Criollo A, Albornoz A, Alfaro IE, Budini M. Chaperone Mediated Autophagy Degrades TDP-43 Protein and Is Affected by TDP-43 Aggregation. Front Mol Neurosci. 2020;13:19. Epub 20200218. doi: 10.3389/fnmol.2020.00019. PubMed PMID: 32132902; PMCID: PMC7040037.
26. Leibiger C, Deisel J, Aufschnaiter A, Ambros S, Tereshchenko M, Verheijen BM, Buttner S, Braun RJ. TDP-43 controls lysosomal pathways thereby determining its own clearance and cytotoxicity. Hum Mol Genet. 2018;27(9):1593-607. doi: 10.1093/hmg/ddy066. PubMed PMID: 29474575.
27. Farias GG, Guardia CM, De Pace R, Britt DJ, Bonifacino JS. BORC/kinesin-1 ensemble drives polarized transport of lysosomes into the axon. Proc Natl Acad Sci U S A. 2017;114(14):E2955-E64. Epub 20170320. doi: 10.1073/pnas.1616363114. PubMed PMID: 28320970; PMCID: PMC5389300.
28. Liao YC, Fernandopulle MS, Wang G, Choi H, Hao L, Drerup CM, Patel R, Qamar S, Nixon-Abell J, Shen Y, Meadows W, Vendruscolo M, Knowles TPJ, Nelson M, Czekalska MA, Musteikyte G, Gachechiladze MA, Stephens CA, Pasolli HA, Forrest LR, St George-Hyslop P, Lippincott-Schwartz J, Ward ME. RNA Granules Hitchhike on Lysosomes for Long-Distance Transport, Using Annexin A11 as a Molecular Tether. Cell. 2019;179(1):147-64 e20. doi: 10.1016/j.cell.2019.08.050. PubMed PMID: 31539493; PMCID: PMC6890474.
29. De Pace R, Ghosh S, Ryan VH, Sohn M, Jarnik M, Rezvan Sangsari P, Morgan NY, Dale RK, Ward ME, Bonifacino JS. Messenger RNA transport on lysosomal vesicles maintains axonal mitochondrial homeostasis and prevents axonal degeneration. Nat Neurosci. 2024;27(6):1087-102. Epub 20240410. doi: 10.1038/s41593-024-01619-1. PubMed PMID: 38600167; PMCID: PMC11156585.
30. Mehta PR, Brown AL, Ward ME, Fratta P. The era of cryptic exons: implications for ALS-FTD. Mol Neurodegener. 2023;18(1):16. Epub 20230315. doi: 10.1186/s13024-023-00608-5. PubMed PMID: 36922834; PMCID: PMC10018954.
31. Gittings LM, Alsop EB, Antone J, Singer M, Whitsett TG, Sattler R, Van Keuren-Jensen K. Cryptic exon detection and transcriptomic changes revealed in single-nuclei RNA sequencing of C9ORF72 patients spanning the ALS-FTD spectrum. Acta Neuropathol. 2023;146(3):433-50. Epub 20230719. doi: 10.1007/s00401-023-02599-5. PubMed PMID: 37466726; PMCID: PMC10412668.
32. Cao MC, Ryan B, Wu J, Curtis MA, Faull RLM, Dragunow M, Scotter EL. A panel of TDP-43-regulated splicing events verifies loss of TDP-43 function in amyotrophic lateral sclerosis brain tissue. Neurobiol Dis. 2023;185:106245. Epub 20230730. doi: 10.1016/j.nbd.2023.106245. PubMed PMID: 37527763.
33. Brown AL, Wilkins OG, Keuss MJ, Hill SE, Zanovello M, Lee WC, Bampton A, Lee FCY, Masino L, Qi YA, Bryce-Smith S, Gatt A, Hallegger M, Fagegaltier D, Phatnani H, Consortium NA, Newcombe J, Gustavsson EK, Seddighi S, Reyes JF, Coon SL, Ramos D, Schiavo G, Fisher EMC, Raj T, Secrier M, Lashley T, Ule J, Buratti E, Humphrey J, Ward ME, Fratta P. TDP-43 loss and ALS-risk SNPs drive mis-splicing and depletion of UNC13A. Nature. 2022;603(7899):131-7. Epub 20220223. doi: 10.1038/s41586-022-04436-3. PubMed PMID: 35197628; PMCID: PMC8891020.
34. Seddighi S, Qi YA, Brown AL, Wilkins OG, Bereda C, Belair C, Zhang YJ, Prudencio M, Keuss MJ, Khandeshi A, Pickles S, Kargbo-Hill SE, Hawrot J, Ramos DM, Yuan H, Roberts J, Sacramento EK, Shah SI, Nalls MA, Colon-Mercado JM, Reyes JF, Ryan VH, Nelson MP, Cook

907 CN, Li Z, Screven L, Kwan JY, Mehta PR, Zanovello M, Hallegger M, Shantaraman A, Ping L,
908 Koike Y, Oskarsson B, Staff NP, Duong DM, Ahmed A, Secrier M, Ule J, Jacobson S, Reich DS,
909 Rohrer JD, Malaspina A, Dickson DW, Glass JD, Ori A, Seyfried NT, Maragkakis M, Petrucelli L,
910 Fratta P, Ward ME. Mis-spliced transcripts generate de novo proteins in TDP-43-related
911 ALS/FTD. Sci Transl Med. 2024;16(734):eadg7162. Epub 20240214. doi:
912 10.1126/scitranslmed.adg7162. PubMed PMID: 38277467; PMCID: PMC11325748.
913 35. Imada EL, Wilks C, Langmead B, Marchionni L. REPAC: analysis of alternative
914 polyadenylation from RNA-sequencing data. Genome Biol. 2023;24(1):22. Epub 20230209. doi:
915 10.1186/s13059-023-02865-5. PubMed PMID: 36759904; PMCID: PMC9912678.
916 36. Ruijtenberg S, Hoek TA, Yan X, Tanenbaum ME. Imaging Translation Dynamics of
917 Single mRNA Molecules in Live Cells. Methods Mol Biol. 2018;1649:385-404. doi: 10.1007/978-
918 1-4939-7213-5_26. PubMed PMID: 29130212.
919 37. Snouwaert JN, Church RJ, Jania L, Nguyen M, Wheeler ML, Saintsing A, Mieczkowski
920 P, Manuel de Villena FP, Armao D, Moy SS, Lorenzo DN, Koller BH. A Mutation in the Borcs7
921 Subunit of the Lysosome Regulatory BORC Complex Results in Motor Deficits and Dystrophic
922 Axonopathy in Mice. Cell Rep. 2018;24(5):1254-65. doi: 10.1016/j.celrep.2018.06.118. PubMed
923 PMID: 30067980.
924 38. De Pace R, Britt DJ, Mercurio J, Foster AM, Djavaherian L, Hoffmann V, Abebe D,
925 Bonifacino JS. Synaptic Vesicle Precursors and Lysosomes Are Transported by Different
926 Mechanisms in the Axon of Mammalian Neurons. Cell Rep. 2020;31(11):107775. doi:
927 10.1016/j.celrep.2020.107775. PubMed PMID: 32553155; PMCID: PMC7478246.
928 39. Yordanov TE, Hipolito VEB, Liebscher G, Vogel GF, Stasyk T, Herrmann C, Geley S,
929 Teis D, Botelho RJ, Hess MW, Huber LA. Biogenesis of lysosome-related organelles complex-1
930 (BORC) regulates late endosomal/lysosomal size through PIKfyve-dependent
931 phosphatidylinositol-3,5-bisphosphate. Traffic. 2019;20(9):674-96. doi: 10.1111/tra.12679.
932 PubMed PMID: 31314175; PMCID: PMC6771566.
933 40. Wu K, Zou J, Sack MN. The endo-lysosomal regulatory protein BLOC1S1 modulates
934 hepatic lysosomal content and lysosomal lipolysis. Biochem Biophys Res Commun. 2023;642:1-
935 10. Epub 20221214. doi: 10.1016/j.bbrc.2022.12.038. PubMed PMID: 36535215; PMCID:
936 PMC9852072.
937 41. de Araujo MEG, Liebscher G, Hess MW, Huber LA. Lysosomal size matters. Traffic.
938 2020;21(1):60-75. Epub 20191206. doi: 10.1111/tra.12714. PubMed PMID: 31808235; PMCID:
939 PMC6972631.
940 42. Jia R, Guardia CM, Pu J, Chen Y, Bonifacino JS. BORC coordinates encounter and
941 fusion of lysosomes with autophagosomes. Autophagy. 2017;13(10):1648-63. Epub 20170821.
942 doi: 10.1080/15548627.2017.1343768. PubMed PMID: 28825857; PMCID: PMC5640200.
943 43. Farfel-Becker T, Roney JC, Cheng XT, Li S, Cuddy SR, Sheng ZH. Neuronal Soma-
944 Derived Degradative Lysosomes Are Continuously Delivered to Distal Axons to Maintain Local
945 Degradation Capacity. Cell Rep. 2019;28(1):51-64 e4. doi: 10.1016/j.celrep.2019.06.013.
946 PubMed PMID: 31269450; PMCID: PMC6696943.
947 44. Nicolas A, Kenna KP, Renton AE, Ticozzi N, Faghri F, Chia R, Dominov JA, Kenna BJ,
948 Nalls MA, Keagle P, Rivera AM, van Rheenen W, Murphy NA, van Vugt J, Geiger JT, Van der
949 Spek RA, Pliner HA, Shankaracharya, Smith BN, Marangi G, Topp SD, Abramzon Y, Gkazi AS,
950 Eicher JD, Kenna A, Consortium I, Mora G, Calvo A, Mazzini L, Riva N, Mandrioli J, Caponnetto
951 C, Battistini S, Volanti P, La Bella V, Conforti FL, Borghero G, Messina S, Simone IL, Trojsi F,
952 Salvi F, Logullo FO, D'Alfonso S, Corrado L, Capasso M, Ferrucci L, Genomic Translation for
953 ALSCC, Moreno CAM, Kamalakaran S, Goldstein DB, Consortium ALSS, Gitler AD, Harris T,
954 Myers RM, Consortium NA, Phatnani H, Musunuri RL, Evani US, Abhyankar A, Zody MC,
955 Answer ALSF, Kaye J, Finkbeiner S, Wyman SK, LeNail A, Lima L, Fraenkel E, Svendsen CN,
956 Thompson LM, Van Eyk JE, Berry JD, Miller TM, Kolb SJ, Cudkowicz M, Baxi E, Clinical
957 Research in ALS, Related Disorders for Therapeutic Development C, Benatar M, Taylor JP,

958 Rampersaud E, Wu G, Wuu J, Consortium S, Lauria G, Verde F, Fogh I, Tiloca C, Comi GP,
959 Soraru G, Cereda C, French ALSC, Corcia P, Laaksovirta H, Myllykangas L, Jansson L, Valori
960 M, Ealing J, Hamdalla H, Rollinson S, Pickering-Brown S, Orrell RW, Sidle KC, Malaspina A,
961 Hardy J, Singleton AB, Johnson JO, Arepalli S, Sapp PC, McKenna-Yasek D, Polak M, Asress
962 S, Al-Sarraj S, King A, Troakes C, Vance C, de Belleroche J, Baas F, Ten Asbroek A, Munoz-
963 Blanco JL, Hernandez DG, Ding J, Gibbs JR, Scholz SW, Floeter MK, Campbell RH, Landi F,
964 Bowser R, Pulst SM, Ravits JM, MacGowan DJL, Kirby J, Pioro EP, Pamphlett R, Broach J,
965 Gerhard G, Dunckley TL, Brady CB, Kowall NW, Troncoso JC, Le Ber I, Mouzat K, Lumbroso S,
966 Heiman-Patterson TD, Kamel F, Van Den Bosch L, Baloh RH, Strom TM, Meitinger T, Shatunov
967 A, Van Eijk KR, de Carvalho M, Kooyman M, Middelkoop B, Moisse M, McLaughlin RL, Van Es
968 MA, Weber M, Boylan KB, Van Blitterswijk M, Rademakers R, Morrison KE, Basak AN, Mora
969 JS, Drory VE, Shaw PJ, Turner MR, Talbot K, Hardiman O, Williams KL, Fifita JA, Nicholson
970 GA, Blair IP, Rouleau GA, Esteban-Perez J, Garcia-Redondo A, Al-Chalabi A, Project Min
971 EALSSC, Rogaeva E, Zinman L, Ostrow LW, Maragakis NJ, Rothstein JD, Simmons Z, Cooper-
972 Knock J, Brice A, Goutman SA, Feldman EL, Gibson SB, Taroni F, Ratti A, Gellera C, Van
973 Damme P, Robberecht W, Fratta P, Sabatelli M, Lunetta C, Ludolph AC, Andersen PM,
974 Weishaupt JH, Camu W, Trojanowski JQ, Van Deerlin VM, Brown RH, Jr., van den Berg LH,
975 Veldink JH, Harms MB, Glass JD, Stone DJ, Tienari P, Silani V, Chio A, Shaw CE, Traynor BJ,
976 Landers JE. Genome-wide Analyses Identify KIF5A as a Novel ALS Gene. Neuron.
977 2018;97(6):1267-88. doi: 10.1016/j.neuron.2018.02.027. PubMed PMID: 29566793; PMCID:
978 PMC5867896.
979 45. De Pace R, Maroofian R, Paimboeuf A, Zamani M, Zaki MS, Sadeghian S, Azizimalamiri
980 R, Galehdari H, Zeighami J, Williamson CD, Fleming E, Zhou D, Gannon JL, Thiffault I, Roze E,
981 Suri M, Zifarelli G, Bauer P, Houlden H, Severino M, Patten SA, Farrow E, Bonifacino JS.
982 Biallelic BORCS8 variants cause an infantile-onset neurodegenerative disorder with altered
983 lysosome dynamics. Brain. 2024;147(5):1751-67. doi: 10.1093/brain/awad427. PubMed PMID:
984 38128568; PMCID: PMC11068110.
985 46. Yang C, Wang H, Qiao T, Yang B, Aliaga L, Qiu L, Tan W, Salameh J, McKenna-Yasek
986 DM, Smith T, Peng L, Moore MJ, Brown RH, Jr., Cai H, Xu Z. Partial loss of TDP-43 function
987 causes phenotypes of amyotrophic lateral sclerosis. Proc Natl Acad Sci U S A.
988 2014;111(12):E1121-9. Epub 20140310. doi: 10.1073/pnas.1322641111. PubMed PMID:
989 24616503; PMCID: PMC3970502.
990 47. Lee EB, Lee VM, Trojanowski JQ. Gains or losses: molecular mechanisms of TDP43-
991 mediated neurodegeneration. Nat Rev Neurosci. 2011;13(1):38-50. Epub 20111130. doi:
992 10.1038/nrn3121. PubMed PMID: 22127299; PMCID: PMC3285250.
993 48. Fernandopulle MS, Prestil R, Grunseich C, Wang C, Gan L, Ward ME. Transcription
994 Factor-Mediated Differentiation of Human iPSCs into Neurons. Curr Protoc Cell Biol.
995 2018;79(1):e51. Epub 20180518. doi: 10.1002/cpcb.51. PubMed PMID: 29924488; PMCID:
996 PMC6993937.
997 49. Wang C, Ward ME, Chen R, Liu K, Tracy TE, Chen X, Xie M, Sohn PD, Ludwig C,
998 Meyer-Franke A, Karch CM, Ding S, Gan L. Scalable Production of iPSC-Derived Human
999 Neurons to Identify Tau-Lowering Compounds by High-Content Screening. Stem Cell Reports.
1000 2017;9(4):1221-33. Epub 20170928. doi: 10.1016/j.stemcr.2017.08.019. PubMed PMID:
1001 28966121; PMCID: PMC5639430.
1002 50. Wang B, Wang M, Zhang W, Xiao T, Chen CH, Wu A, Wu F, Traugh N, Wang X, Li Z,
1003 Mei S, Cui Y, Shi S, Lipp JJ, Hinterndorfer M, Zuber J, Brown M, Li W, Liu XS. Integrative
1004 analysis of pooled CRISPR genetic screens using MAGeCKFlute. Nat Protoc. 2019;14(3):756-
1005 80. Epub 20190201. doi: 10.1038/s41596-018-0113-7. PubMed PMID: 30710114; PMCID:
1006 PMC6862721.
1007 51. Carpenter AE, Jones TR, Lamprecht MR, Clarke C, Kang IH, Friman O, Guertin DA,
1008 Chang JH, Lindquist RA, Moffat J, Golland P, Sabatini DM. CellProfiler: image analysis software

1009 for identifying and quantifying cell phenotypes. Genome Biol. 2006;7(10):R100. Epub 20061031.
1010 doi: 10.1186/gb-2006-7-10-r100. PubMed PMID: 17076895; PMCID: PMC1794559.
1011 52. Livak KJ, Schmittgen TD. Analysis of relative gene expression data using real-time
1012 quantitative PCR and the 2(-Delta Delta C(T)) Method. Methods. 2001;25(4):402-8. doi:
1013 10.1006/meth.2001.1262. PubMed PMID: 11846609.
1014 53. Goedhart J, Luijsterburg MS. VolcaNoseR is a web app for creating, exploring, labeling
1015 and sharing volcano plots. Sci Rep. 2020;10(1):20560. Epub 20201125. doi: 10.1038/s41598-
1016 020-76603-3. PubMed PMID: 33239692; PMCID: PMC7689420.
1017 54. Ge SX, Jung D, Yao R. ShinyGO: a graphical gene-set enrichment tool for animals and
1018 plants. Bioinformatics. 2020;36(8):2628-9. doi: 10.1093/bioinformatics/btz931. PubMed PMID:
1019 31882993; PMCID: PMC7178415.
1020 55. Dobin A, Davis CA, Schlesinger F, Drenkow J, Zaleski C, Jha S, Batut P, Chaisson M,
1021 Gingeras TR. STAR: ultrafast universal RNA-seq aligner. Bioinformatics. 2013;29(1):15-21.
1022 Epub 20121025. doi: 10.1093/bioinformatics/bts635. PubMed PMID: 23104886; PMCID:
1023 PMC3530905.
1024 56. Vaquero-Garcia J, Barrera A, Gazzara MR, Gonzalez-Vallinas J, Lahens NF,
1025 Hogenesch JB, Lynch KW, Barash Y. A new view of transcriptome complexity and regulation
1026 through the lens of local splicing variations. Elife. 2016;5:e11752. Epub 20160201. doi:
1027 10.7554/eLife.11752. PubMed PMID: 26829591; PMCID: PMC4801060.
1028 57. Molder F, Jablonski KP, Letcher B, Hall MB, Tomkins-Tinch CH, Sochat V, Forster J,
1029 Lee S, Twardziok SO, Kanitz A, Wilm A, Holtgrewe M, Rahmann S, Nahnsen S, Koster J.
1030 Sustainable data analysis with Snakemake. F1000Res. 2021;10:33. Epub 20210118. doi:
1031 10.12688/f1000research.29032.2. PubMed PMID: 34035898; PMCID: PMC8114187.
1032 58. Reilly L, Lara E, Ramos D, Li Z, Pantazis CB, Stadler J, Santiana M, Roberts J, Faghri
1033 F, Hao Y, Nalls MA, Narayan P, Liu Y, Singleton AB, Cookson MR, Ward ME, Qi YA. A fully
1034 automated FAIMS-DIA mass spectrometry-based proteomic pipeline. Cell Rep Methods.
1035 2023;3(10):100593. Epub 20230919. doi: 10.1016/j.crmeth.2023.100593. PubMed PMID:
1036 37729920; PMCID: PMC10626189.
1037 59. Cox J, Mann M. MaxQuant enables high peptide identification rates, individualized
1038 p.p.b.-range mass accuracies and proteome-wide protein quantification. Nat Biotechnol.
1039 2008;26(12):1367-72. Epub 20081130. doi: 10.1038/nbt.1511. PubMed PMID: 19029910.
1040 60. Frankenfield AM, Ni J, Ahmed M, Hao L. Protein Contaminants Matter: Building
1041 Universal Protein Contaminant Libraries for DDA and DIA Proteomics. J Proteome Res.
1042 2022;21(9):2104-13. Epub 20220706. doi: 10.1021/acs.jproteome.2c00145. PubMed PMID:
1043 35793413; PMCID: PMC10040255.
1044 61. Hasan S, Fernandopulle MS, Humble SW, Frankenfield AM, Li H, Prestil R, Johnson KR,
1045 Ryan BJ, Wade-Martins R, Ward ME, Hao L. Multi-modal proteomic characterization of
1046 lysosomal function and proteostasis in progranulin-deficient neurons. Mol Neurodegener.
1047 2023;18(1):87. Epub 20231116. doi: 10.1186/s13024-023-00673-w. PubMed PMID: 37974165;
1048 PMCID: PMC10655356.
1049 62. Kong AT, Leprevost FV, Avtonomov DM, Mellacheruvu D, Nesvizhskii AI. MSFragger:
1050 ultrafast and comprehensive peptide identification in mass spectrometry-based proteomics. Nat
1051 Methods. 2017;14(5):513-20. Epub 20170410. doi: 10.1038/nmeth.4256. PubMed PMID:
1052 28394336; PMCID: PMC5409104.
1053 63. Shteynberg DD, Deutsch EW, Campbell DS, Hoopmann MR, Kusebauch U, Lee D,
1054 Mendoza L, Midha MK, Sun Z, Whetton AD, Moritz RL. PTMProphet: Fast and Accurate Mass
1055 Modification Localization for the Trans-Proteomic Pipeline. J Proteome Res. 2019;18(12):4262-
1056 72. Epub 20190722. doi: 10.1021/acs.jproteome.9b00205. PubMed PMID: 31290668; PMCID:
1057 PMC6898736.
1058 64. da Veiga Leprevost F, Haynes SE, Avtonomov DM, Chang HY, Shanmugam AK,
1059 Mellacheruvu D, Kong AT, Nesvizhskii AI. Philosopher: a versatile toolkit for shotgun proteomics

data analysis. Nat Methods. 2020;17(9):869-70. doi: 10.1038/s41592-020-0912-y. PubMed PMID: 32669682; PMCID: PMC7509848.
65. Perez-Riverol Y, Bai J, Bandla C, Garcia-Seisdedos D, Hewapathirana S, Kamatchinathan S, Kundu DJ, Prakash A, Frericks-Zipper A, Eisenacher M, Walzer M, Wang S, Brazma A, Vizcaino JA. The PRIDE database resources in 2022: a hub for mass spectrometry-based proteomics evidences. Nucleic Acids Res. 2022;50(D1):D543-D52. doi: 10.1093/nar/gkab1038. PubMed PMID: 34723319; PMCID: PMC8728295.

Figures and legends

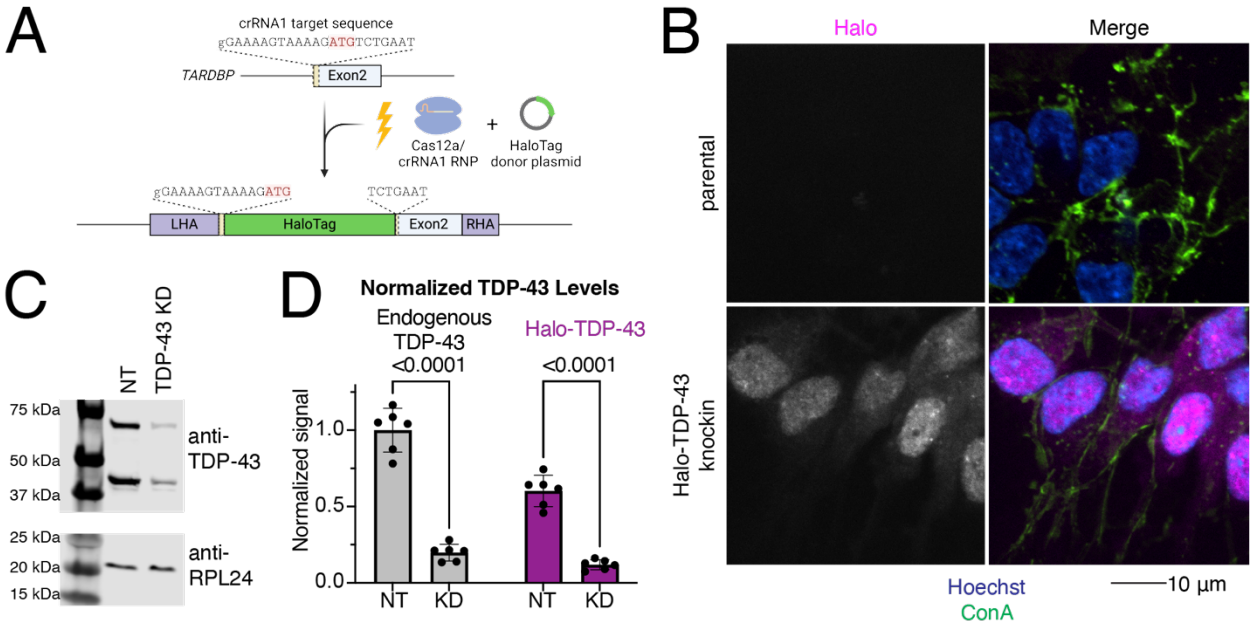

Figure 1: Generation of an endogenously HaloTagged TDP-43 iPSC line.

A) Schematic of knock into the N-terminus of TDP-43. Cas12a-crRNA ribonucleoparticle (RNP) and HaloTag donor plasmid containing homology arms to TDP-43 were nucleofected into iPSCs. Halo was knocked into a single TDP-43 allele at the N-terminus of the protein, before exon 2, just after the start codon (ATG).

B) Microscopy validation of Halo-TDP-43 localization to nucleus. Halo in pink, ConA lipid dye in green, and Hoechst in blue. Halo signal is indicated in grayscale in left panels. Scale bar 10 µm.

C) TDP-43 western blot of NT and TDP-43 KD neurons. Halo-TDP-43 is approximately 33 kDa heavier than untagged TDP-43, which corresponds to the molecular weight of Halo. RPL24 is shown as a loading control. TDP-43 KD decreases levels of both tagged and untagged TDP-43 compared to non-targeting (NT) control sgRNA.

D) Quantification of western blot shown in (C) shows untagged (left) and Halo-Tagged (right) TDP-43 is decreased upon TDP-43 KD. Interestingly, Halo-TDP-43 is expressed at levels about one half as much as untagged TDP-43.

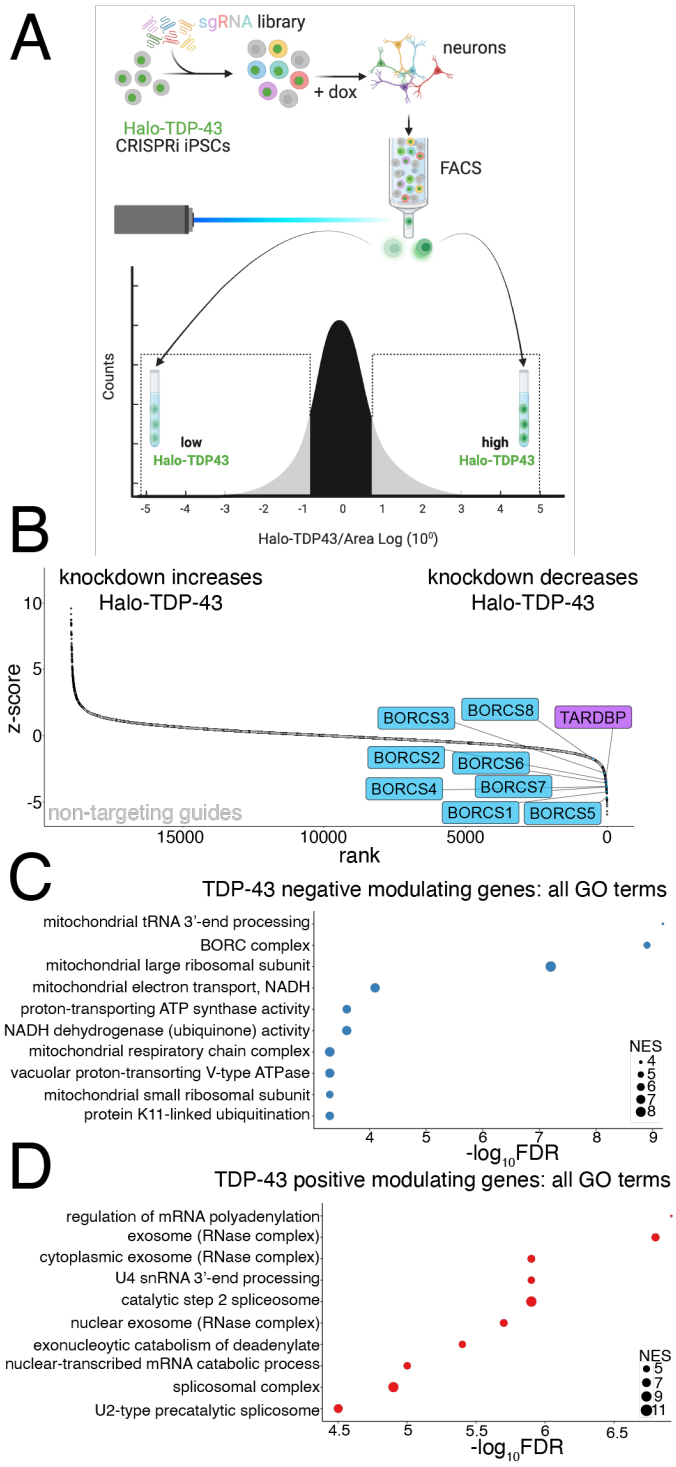

Figure 2: CRISPRi screen identifies modifiers of TDP-43 protein levels in iPSC-derived neurons.

A) Schematic of FACS screen. Halo-TDP-43 iPSCs were transduced with the dual guide library and selected. After selection, iPSCs were differentiated to neurons via Dox-inducible NGN2 expression. Neurons were FACS sorted and populations expressing high Halo-TDP-43 and low Halo-TDP-43 were collected, DNA extracted, and sgRNA libraries sequenced.

1093 B) Rank plot of screen results showing genes whose KD increases Halo-TDP-43 levels
1094 (left) and genes whose KD decreases Halo-TDP-43 levels, including TDP-43 itself
1095 (right). BORC genes are in blue. Non-targeting guides are indicated in gray and cluster
1096 in the middle, linear portion of the graph, demarking genes that do not change Halo-
1097 TDP-43 levels.
1098 C) GO analysis of screen hits that reduce Halo-TDP-43 levels include the BORC complex
1099 and many mitochondria-associated terms. The FDR is from the calculated permutation p
1100 value of 1000 iterations.
1101 D) GO analysis of screen hits that increase Halo-TDP-43 levels include many hits related to
1102 mRNA processing. The FDR is from the calculated permutation p value of 1000
1103 iterations.

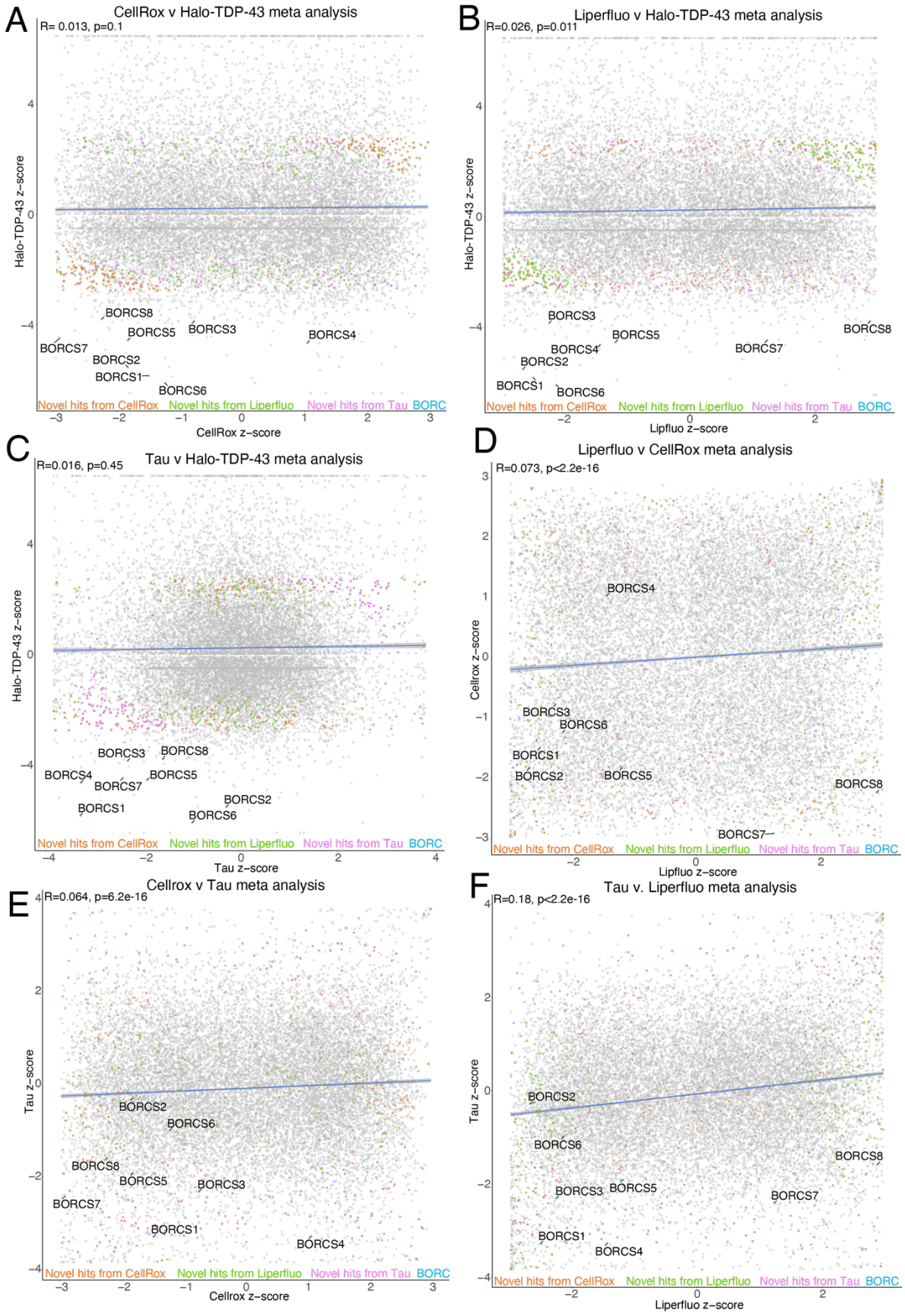
A
CellRox v Halo-TDP-43 meta analysis
R= 0.013, p=0.1
Halo-TDP-43 z−score
CellRox z−score
BORCS8
BORCS5
BORCS3
BORCS4
BORCS7
BORCS2
BORCS1
BORCS6
Novel hits from CellRox
Novel hits from Liperfluo
Novel hits from Tau
BORC
B
Liperfluo v Halo-TDP-43 meta analysis
R=0.026, p=0.011
Halo-TDP-43 z−score
Lipfluo z−score
BORCS3
BORCS5
BORCS8
BORCS4
BORCS7
BORCS2
BORCS1
BORCS6
Novel hits from CellRox
Novel hits from Liperfluo
Novel hits from Tau
BORC
C
Tau v Halo-TDP-43 meta analysis
R=0.016, p=0.45
Halo-TDP-43 z−score
Tau z−score
BORCS3
BORCS8
BORCS4
BORCS5
BORCS7
BORCS2
BORCS1
BORCS6
Novel hits from CellRox
Novel hits from Liperfluo
Novel hits from Tau
BORC
D
Liperfluo v CellRox meta analysis
R=0.073, p<2.2e-16
Cellrox z−score
Lipfluo z−score
BORCS4
BORCS3
BORCS6
BORCS1
BORCS2
BORCS5
BORCS8
BORCS7
Novel hits from CellRox
Novel hits from Liperfluo
Novel hits from Tau
BORC
E
Cellrox v Tau meta analysis
R=0.064, p=6.2e-16
Tau z−score
Cellrox z−score
BORCS2
BORCS6
BORCS8
BORCS5
BORCS3
BORCS7
BORCS1
BORCS4
Novel hits from CellRox
Novel hits from Liperfluo
Novel hits from Tau
BORC
F
Tau v. Liperfluo meta analysis
R=0.18, p<2.2e-16
Tau z−score
Liperfluo z−score
BORCS2
BORCS6
BORCS8
BORCS3
BORCS5
BORCS7
BORCS1
BORCS4
Novel hits from CellRox
Novel hits from Liperfluo
Novel hits from Tau
BORC

1104

Figure 3: Meta-analysis of CRISPRi screens identifies novel and common genes.

A) Comparison between CellRox and Halo-TDP-43 meta-analysis z-scores with novel hits highlighted. Correlation is indicated in blue with R and p-value at top left of graph. BORC genes are highlighted in blue, novel hits from Liperfluo, CellRox, and Tau screens as compared to our Halo-TDP-43 screen are indicated in green, orange, and pink, respectively.

B) Comparison between Liperfluo and Halo-TDP-43 meta-analysis z-scores with novel hits highlighted. Correlation is indicated in blue with R and p-value at top left of graph. BORC genes are highlighted in blue, novel hits from Liperfluo, CellRox, and Tau screens as compared to our Halo-TDP-43 screen are indicated in green, orange, and pink, respectively. Comparison between Tau and Halo-TDP-43 meta-analysis z-scores with novel hits highlighted. BORC genes are highlighted in light blue. Correlation is indicated in blue with R and p-value at top left of graph.

C) Comparison between Tau and Halo-TDP-43 meta-analysis z-scores with novel hits highlighted. Correlation is indicated in blue with R and p-value at top left of graph. BORC genes are highlighted in blue, novel hits from Liperfluo, CellRox, and Tau screens as compared to our Halo-TDP-43 screen are indicated in green, orange, and pink, respectively.

D) Comparison between Liperfluo and CellRox meta-analysis z-scores with novel hits highlighted. Correlation is indicated in blue with R and p-value at top left of graph. BORC genes are highlighted in blue, novel hits from Liperfluo, CellRox, and Tau screens as compared to our Halo-TDP-43 screen are indicated in green, orange, and pink, respectively.

E) Comparison between CellRox and Tau meta-analysis z-scores with novel hits highlighted. Correlation is indicated in blue with R and p-value at top left of graph. BORC genes are highlighted in blue, novel hits from Liperfluo, CellRox, and Tau screens as compared to our Halo-TDP-43 screen are indicated in green, orange, and pink, respectively.

F) Comparison between Tau and Liperfluo meta-analysis z-scores with novel hits highlighted. Correlation is indicated in blue with R and p-value at top left of graph. BORC genes are highlighted in blue, novel hits from Liperfluo, CellRox, and Tau screens as compared to our Halo-TDP-43 screen are indicated in green, orange, and pink, respectively.

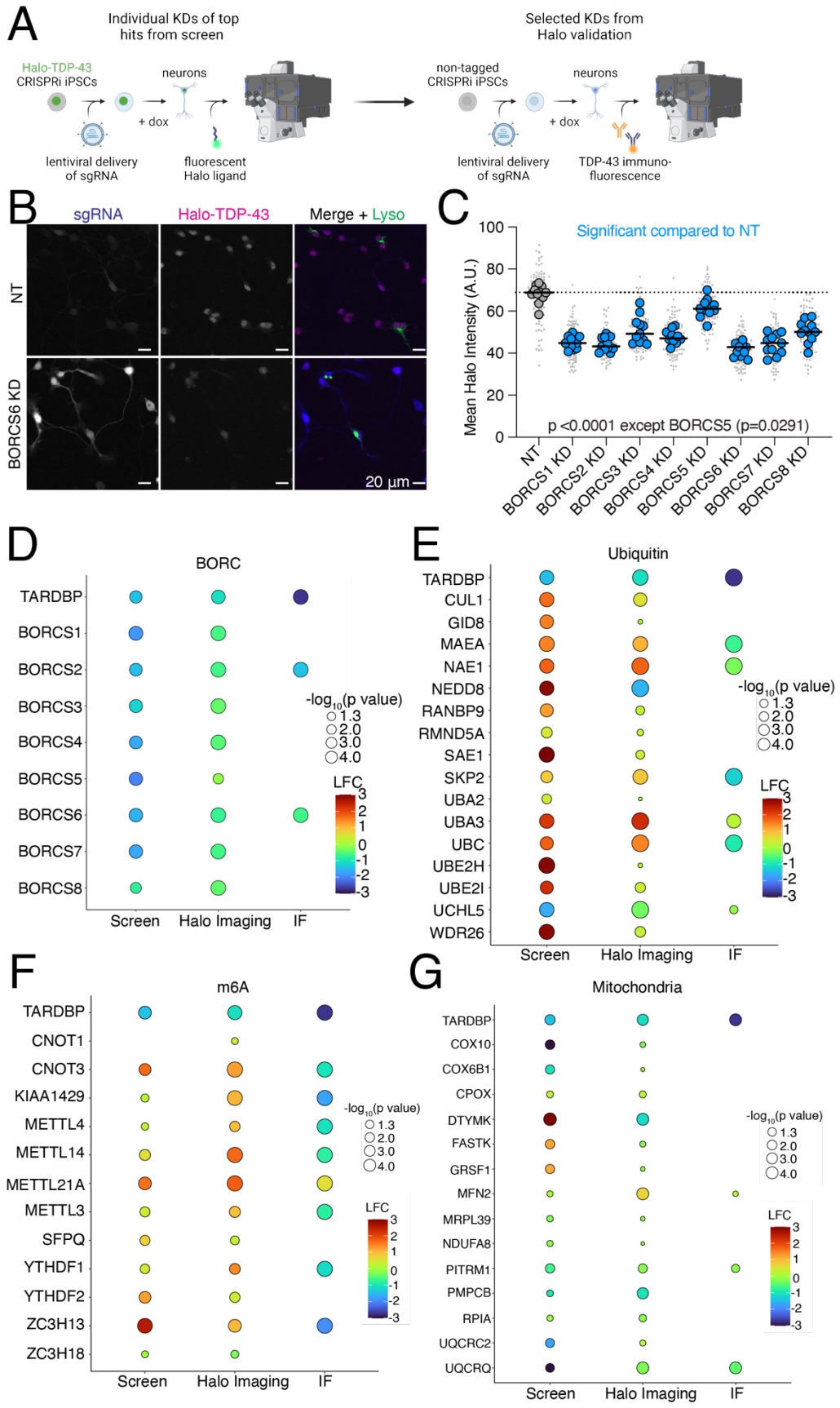
A
Individual KDs of top hits from screen
Halo-TDP-43 CRISPRi iPSCs
neurons
+ dox
lentiviral delivery of sgRNA
fluorescent Halo ligand
Selected KDs from Halo validation
non-tagged CRISPRi iPSCs
neurons
+ dox
lentiviral delivery of sgRNA
TDP-43 immuno-fluorescence
B
sgRNA
Halo-TDP-43
Merge + Lyso
NT
BORCS6 KD
20 µm
C
Significant compared to NT
Mean Halo Intensity (A.U.)
p <0.0001 except BORCS5 (p=0.0291)
NT
BORCS1 KD
BORCS2 KD
BORCS3 KD
BORCS4 KD
BORCS5 KD
BORCS6 KD
BORCS7 KD
BORCS8 KD
D
BORC
TARDBP
BORCS1
BORCS2
BORCS3
BORCS4
BORCS5
BORCS6
BORCS7
BORCS8
Screen
Halo Imaging
IF
-log10(p value)
LFC
E
Ubiquitin
TARDBP
CUL1
GID8
MAEA
NAE1
NEDD8
RANBP9
RMND5A
SAE1
SKP2
UBA2
UBA3
UBC
UBE2H
UBE2I
UCHL5
WDR26
Screen
Halo Imaging
IF
-log10(p value)
LFC
F
m6A
TARDBP
CNOT1
CNOT3
KIAA1429
METTL4
METTL14
METTL21A
METTL3
SFPQ
YTHDF1
YTHDF2
ZC3H13
ZC3H18
Screen
Halo Imaging
IF
-log10(p value)
LFC
G
Mitochondria
TARDBP
COX10
COX6B1
CPOX
DTYMK
FASTK
GRSF1
MFN2
MRPL39
NDUFA8
PITRM1
PMPCB
RPIA
UQCRC2
UQCRQ
Screen
Halo Imaging
IF
-log10(p value)
LFC

1138

1139 Figure 4: Validation of modulators of TDP-43 levels in iPSC-derived neurons.

1140 A) Schematic of hit validation. As a first validation, Halo-TDP-43 iPSCs were transduced
1141 with single sgRNAs against hit genes and Halo levels were analyzed by microscopy,
1142 generating a list of Halo-validated hits. Then some genes were selected from the Halo-
1143 validated hits and untagged iPSCs were transduced with the same virus and TDP-43
1144 protein levels assessed via TDP-43 immunofluorescence microscopy, identifying hits not
1145 affected by a HaloTag.

1146 B) Representative images of Halo-TDP-43 live cell imaging with BORCS6 KD. sgRNA
1147 plasmids contain a cytoplasmic BFP, enabling identification of cells expressing the
1148 sgRNA. For BORC genes, iPSCs were transduced with a lysosome marker (LAMP1-
1149 mApple) to ensure functional BORC KD through depletion of neuritic lysosomes. Scale
1150 bar represents 20 µm.

1151 C) Quantification of BORC KD Halo-TDP-43 microscopy. All BORC genes tested (S1-S8)
1152 showed statistically significant decreases in Halo-TDP-43 levels compared to a non-
1153 targeting (NT) guide, indicated by blue dots. N=12 wells per genotype, 9 images per well
1154 (small gray dots). Significant p-values indicated on graph.

1155 D) (D-G) Summary graphs of screen, Halo live cell imaging, and TDP-43
1156 immunofluorescence imaging fold changes for (D) BORC KD,

1157 E) (E) Ubiquitin-associated gene KD,

1158 F) (F) m6A-associated gene KD, and

1159 G) (G) mitochondria gene KDs. Color indicates strength of $\log_2$FoldChange for each
1160 condition, circle size indicates -$\log_{10}$p-value; values below 1.3 are not significant,
1161 corresponding to a p-value of 0.05. No circle indicates the gene was not tested in that
1162 experiment (i.e., not all genes were tested by immunofluorescence).

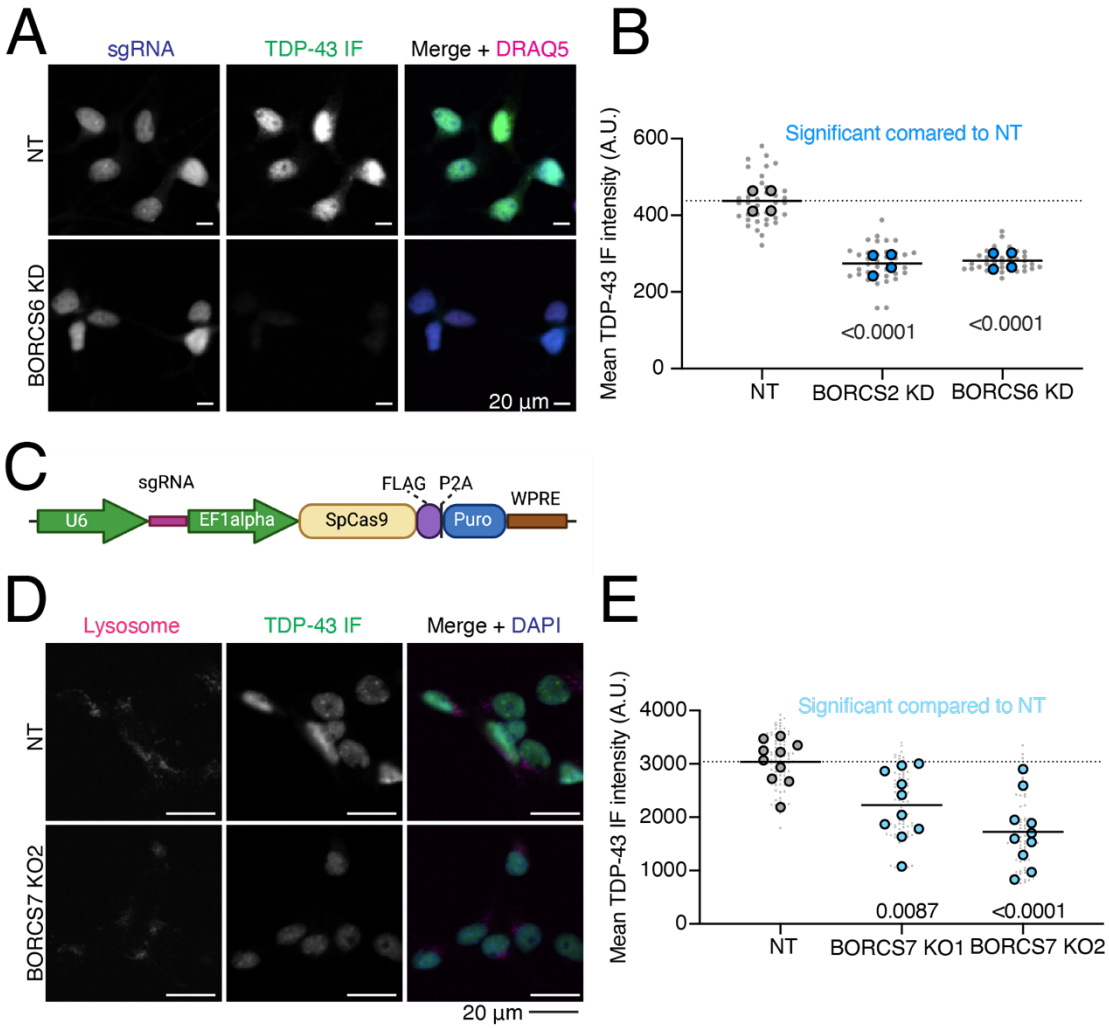

Figure 5: Endogenous validation of TDP-43 level modifiers in iPSC-derived neurons.

A) Quantification of BORC KD TDP-43 immunofluorescence microscopy. Both BORC genes tested (S2 and S6) show significant decreases in untagged TDP-43 levels compared to a NT guide, indicated by blue dots. N=4 wells per genotype, 9 images per well (small gray dots). Significant p-values indicated on graph.

B) Representative images of TDP-43 immunofluorescence imaging with BORCS6 KD. sgRNA plasmids contain a cytoplasmic BFP, enabling identification of cells expressing the sgRNA. Scale bar represents 20 µm.

C) Schematic of pLentiCRISPR plasmid. pLentiCRISPR enables lentiviral delivery of a plasmid expressing an sgRNA of interest under a U6 promoter and Cas9 under an Ef1alpha promoter. This enables knockout of a gene of interest targeted by an sgRNA.

D) Representative images of BORCS7 KO TDP-43 IF with lysosomes stained with anti-H4A3 antibody. Scale bar is 20 µm.

E) Quantification of TDP-43 immunofluorescence on BORCS7 knockout neurons. Both BORCS7 guides significantly reduced the amount of TDP-43 IF signal compared to a NT guide, light blue dots. N=10 wells, 9 images per well (light gray dots). Significant p-values indicated on graph.

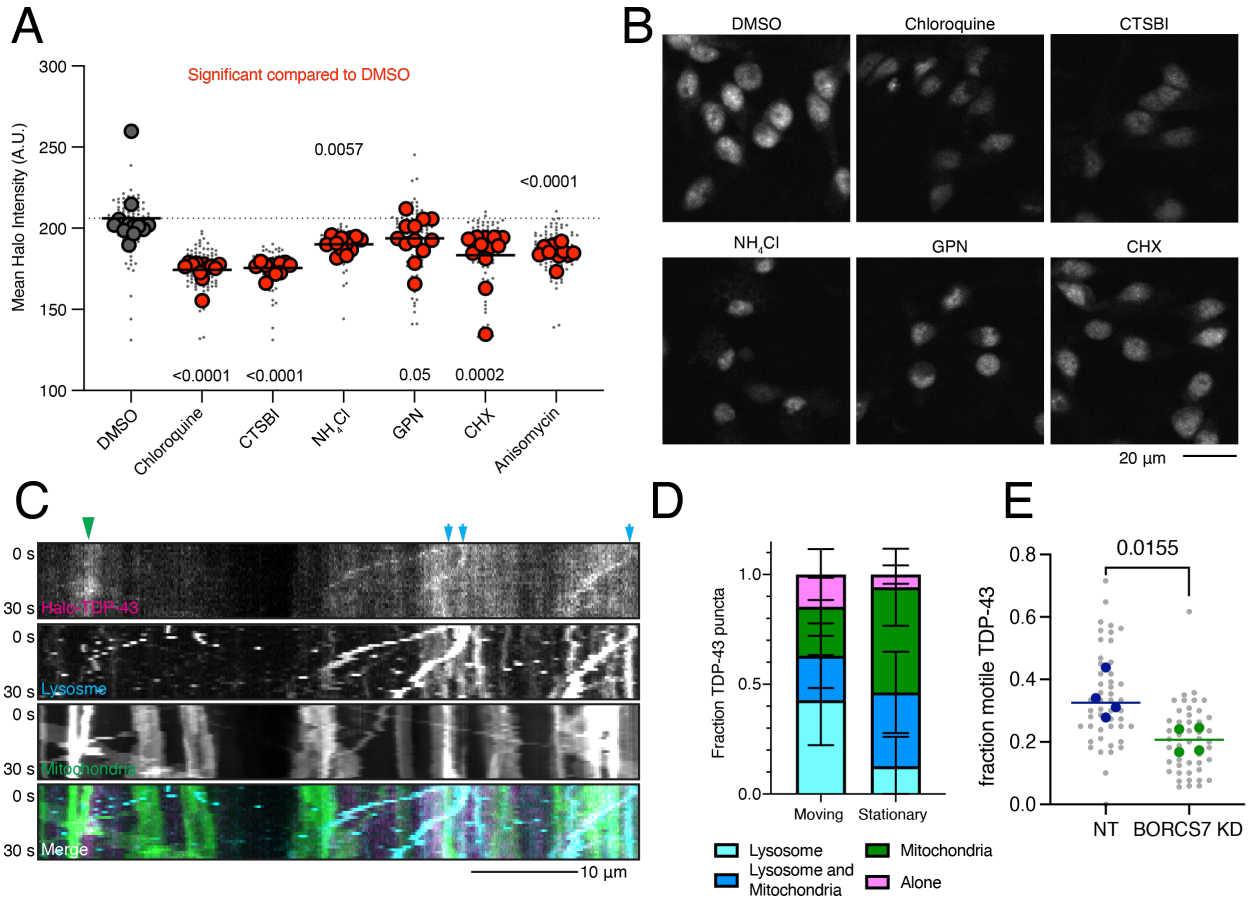

Figure 6: TDP-43 protein levels require active and neuritically localized lysosomes.

A) Drugs targeting different aspects of lysosome function decrease Halo-TDP-43 levels. All drugs tested were significant compared to a DMSO treatment, indicated by red dots. N=12 wells, 9 images per well (small grey dots), mean of each well is indicated by large dot.

B) Representative images of drug treatments that decrease Halo-TDP-43 levels. Scale bar is 20 µm.

C) Representative 30 s kymographs of Halo-TDP-43, lysosomes (LAMP1-mApple), mitochondria (mito-mEmerald), showing co-transport of Halo-TDP-43 with organelles. Green arrowhead indicates co-localization with static mitochondria; blue arrows indicate co-localization with motile lysosomes. Scale bar is 10 µm.

D) Quantification of Halo-TDP-43 signal with organelles. Motile Halo-TDP-43 in neurites is primarily co-transported with lysosomes or lysosomes and mitochondria together. Stationary Halo-TDP-43 is more likely to be associated with mitochondria.

E) Upon BORCS7 KD, TDP-43 is less mobile compared to a NT guide, likely due to restriction of lysosomes to the soma. N=4 wells (mean per well indicated by large dot), 8 images per well (small dots).

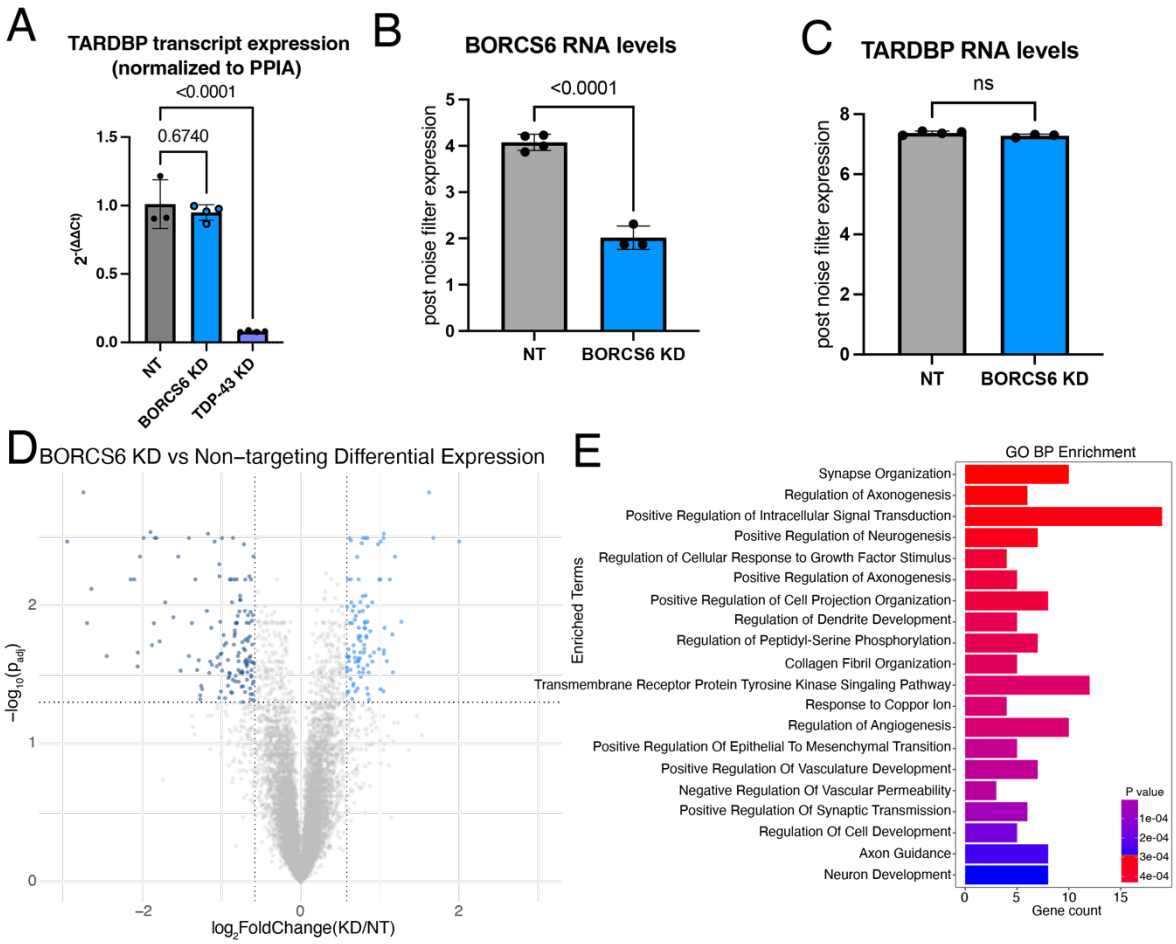

Figure 7: BORC KD does not affect TDP-43 RNA levels.

A) qPCR of NT, BORCS6 KD, and TDP-43 KD neurons showing decreased TDP-43 mRNA levels in TDP-43 KD, but not BORCS6 KD. Normalized to PPIA. NT n=3, BORCS6 KD n=4, and TDP-43 KD n=4.
B) Normalized transcript counts of NT and BORCS6 KD neurons showing about half as much BORCS6 mRNA in BORCS6 KD neurons. NT n=4, BORCS6 KD n=3.
C) Normalized transcript counts of NT and BORCS6 KD neurons showing no change in TARDBP (TDP-43) mRNA levels in BORCS6 KD neurons. NT n=4, BORCS6 KD n=3.
D) Volcano plot comparing BORCS6 KD with NT neurons. 98 genes increase expression upon BORCS6 KD (right of graph), while 139 genes decrease expression (left of graph). NT n=4, BORCS6 KD n=3.
E) GO BP enrichment analysis from Enrichr of genes significantly altered in BORCS6 KD neurons compared to NT neurons shows several neuron and axon related terms.

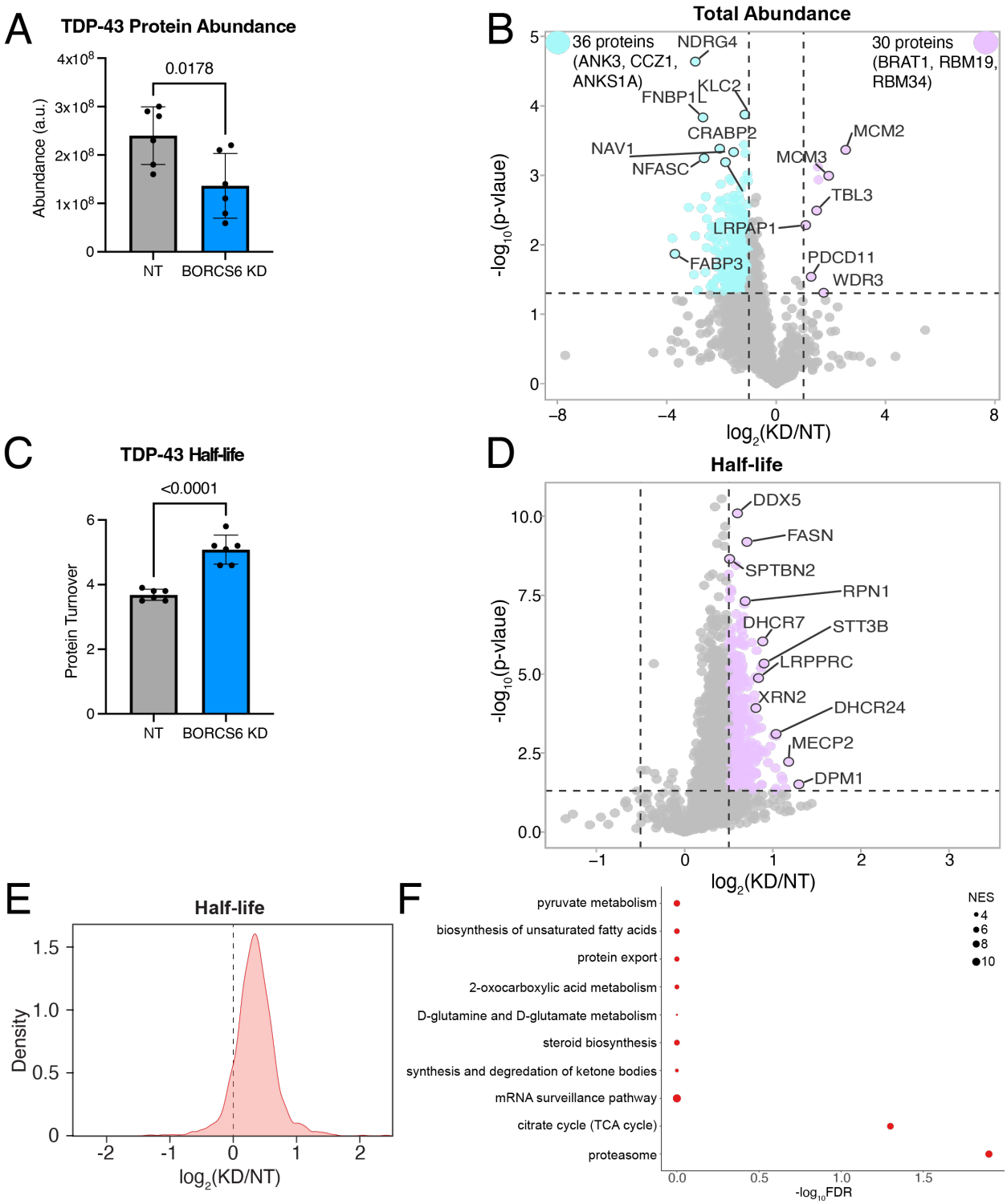

Figure 8: BORC KD alters the abundance and half-lives of TDP-43 and other proteins.

A) TDP-43 protein has decreased total abundance in day 7 BORCS6 neurons.

B) Volcano plot of total protein abundance comparing BORCS6 KD to a non-targeting guide. Some proteins (purple) have increased abundance, while a larger number (teal) have decreased abundance. Non-significant or low $\log_2$(fold change) proteins are

1219 indicated in grey. Vertical lines at log_2(fold change) of 1 and -1, horizontal line at p-value
1220 = 0.05.
1221 C) TDP-43 has longer half-life in day 7 BORCS6 KD neurons.
1222 D) Volcano plot of half-life changes in BORCS6 KD neurons as compared to neurons
1223 expressing a non-targeting guide. Non-significant or low log_2(fold change) protein
1224 turnovers are indicated in grey. Horizontal line at p=0.05, vertical lines at log_2(fold
1225 change) of 0.5 or -0.5.
1226 E) Density plot of global protein turnover shows longer protein half-lives upon BORC KD.
1227 F) Gene ontology enrichment analysis using proteins with longer half-lives in BORCS6 KD
1228 neurons shows KEGG pathways related to protein export, proteasome, and metabolism.
1229

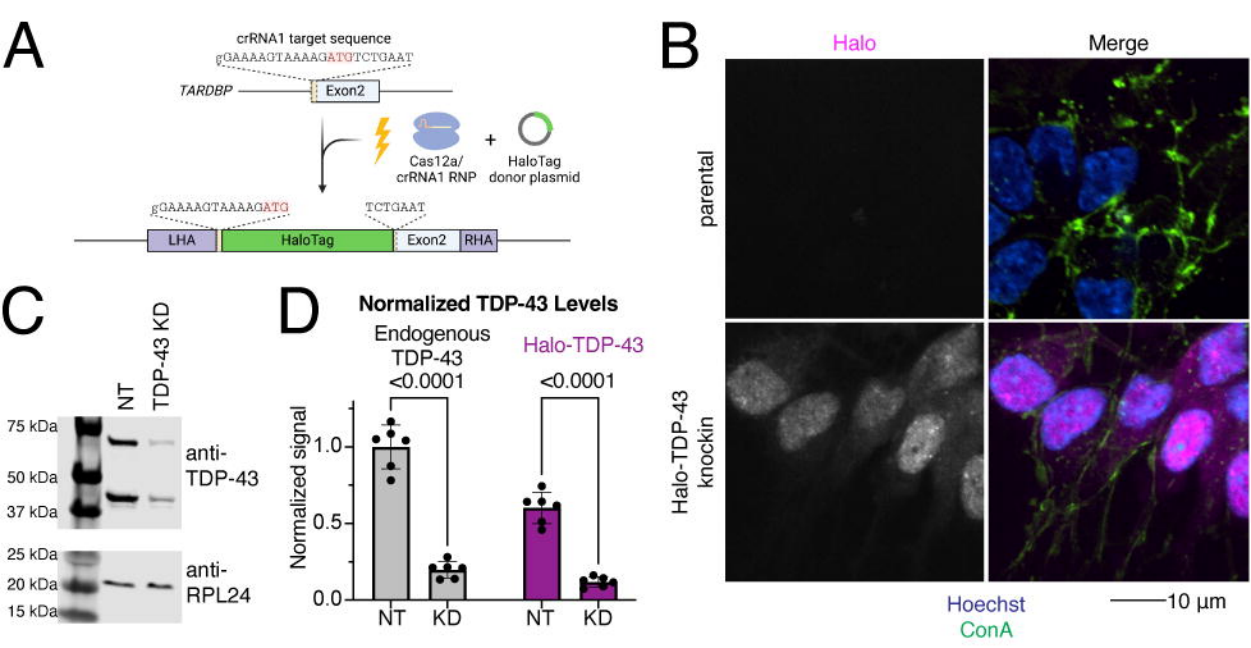
A
crRNA1 target sequence
gGAAAAGTAAAAGATGTCTGAAT
TARDBP
Exon2
Cas12a/
crRNA1 RNP
+
HaloTag
donor plasmid
gGAAAAGTAAAAGATG
TCTGAAT
LHA
HaloTag
Exon2
RHA
B
Halo
Merge
parental
Halo-TDP-43
knockin
Hoechst
ConA
10 µm
C
NT
TDP-43 KD
75 kDa
50 kDa
37 kDa
anti-
TDP-43
25 kDa
20 kDa
15 kDa
anti-
RPL24
D
Normalized TDP-43 Levels
Endogenous
TDP-43
Halo-TDP-43
<0.0001
<0.0001
Normalized signal
1.0
0.5
0.0
NT
KD
NT
KD

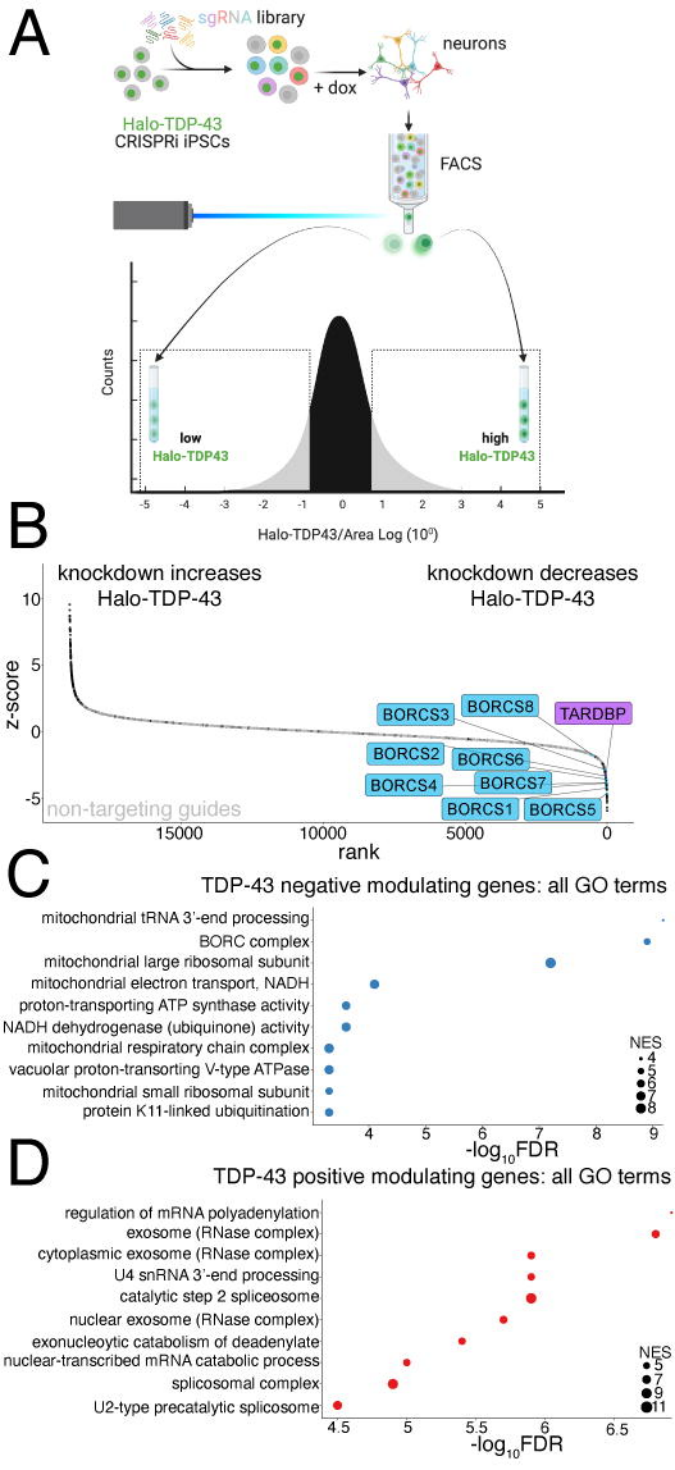
A
sgRNA library
neurons
+ dox
Halo-TDP-43
CRISPRi iPSCs
FACS
Counts
low
Halo-TDP43
high
Halo-TDP43
-5 -4 -3 -2 -1 0 1 2 3 4 5
Halo-TDP43/Area Log (10^0)
B
knockdown increases
Halo-TDP-43
knockdown decreases
Halo-TDP-43
z-score
10
5
0
-5
BORCS3
BORCS8
TARDBP
BORCS2
BORCS6
BORCS4
BORCS7
BORCS1
BORCS5
non-targeting guides
15000
10000
5000
0
rank
C
TDP-43 negative modulating genes: all GO terms
mitochondrial tRNA 3'-end processing
BORC complex
mitochondrial large ribosomal subunit
mitochondrial electron transport, NADH
proton-transporting ATP synthase activity
NADH dehydrogenase (ubiquinone) activity
mitochondrial respiratory chain complex
vacuolar proton-transorting V-type ATPase
mitochondrial small ribosomal subunit
protein K11-linked ubiquitination
NES
4
5
6
7
8
4 5 6 7 8 9
-log10FDR
D
TDP-43 positive modulating genes: all GO terms
regulation of mRNA polyadenylation
exosome (RNase complex)
cytoplasmic exosome (RNase complex)
U4 snRNA 3'-end processing
catalytic step 2 spliceosome
nuclear exosome (RNase complex)
exonucleoytic catabolism of deadenylate
nuclear-transcribed mRNA catabolic process
splicosomal complex
U2-type precatalytic splicosome
NES
5
7
9
11
4.5 5 5.5 6 6.5
-log10FDR

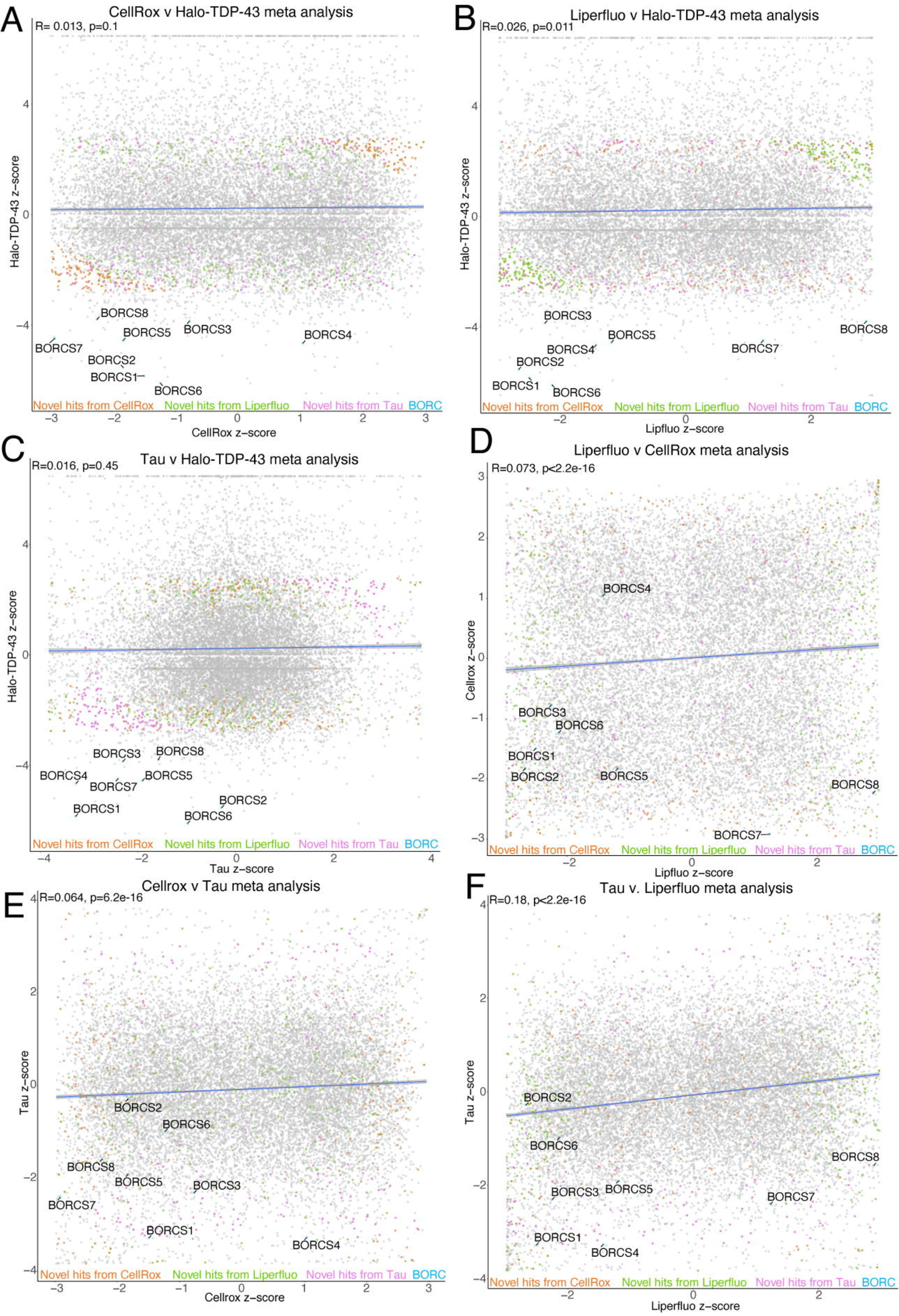
A
CellRox v Halo-TDP-43 meta analysis
R= 0.013, p=0.1
Halo-TDP-43 z−score
CellRox z−score
BORCS8
BORCS5
BORCS3
BORCS4
BORCS7
BORCS2
BORCS1
BORCS6
Novel hits from CellRox
Novel hits from Liperfluo
Novel hits from Tau
BORC
B
Liperfluo v Halo-TDP-43 meta analysis
R=0.026, p=0.011
Halo-TDP-43 z−score
Lipfluo z−score
BORCS3
BORCS5
BORCS8
BORCS4
BORCS7
BORCS2
BORCS1
BORCS6
Novel hits from CellRox
Novel hits from Liperfluo
Novel hits from Tau
BORC
C
Tau v Halo-TDP-43 meta analysis
R=0.016, p=0.45
Halo-TDP-43 z−score
Tau z−score
BORCS3
BORCS8
BORCS4
BORCS5
BORCS7
BORCS2
BORCS1
BORCS6
Novel hits from CellRox
Novel hits from Liperfluo
Novel hits from Tau
BORC
D
Liperfluo v CellRox meta analysis
R=0.073, p<2.2e-16
Cellrox z−score
Lipfluo z−score
BORCS4
BORCS3
BORCS6
BORCS1
BORCS2
BORCS5
BORCS8
BORCS7
Novel hits from CellRox
Novel hits from Liperfluo
Novel hits from Tau
BORC
E
Cellrox v Tau meta analysis
R=0.064, p=6.2e-16
Tau z−score
Cellrox z−score
BORCS2
BORCS6
BORCS8
BORCS5
BORCS3
BORCS7
BORCS1
BORCS4
Novel hits from CellRox
Novel hits from Liperfluo
Novel hits from Tau
BORC
F
Tau v. Liperfluo meta analysis
R=0.18, p<2.2e-16
Tau z−score
Liperfluo z−score
BORCS2
BORCS6
BORCS8
BORCS3
BORCS5
BORCS7
BORCS1
BORCS4
Novel hits from CellRox
Novel hits from Liperfluo
Novel hits from Tau
BORC

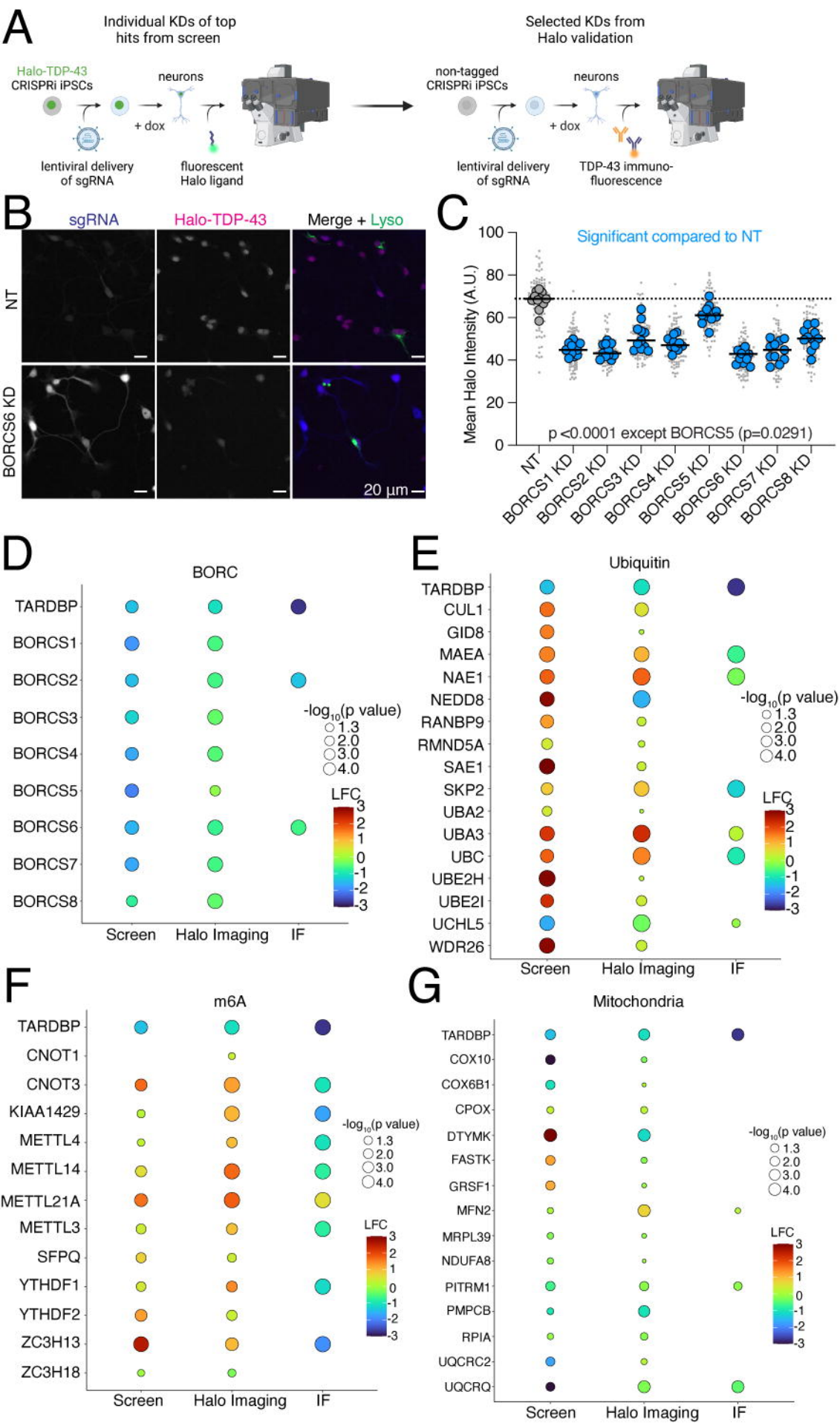
A
Individual KDs of top hits from screen
Halo-TDP-43 CRISPRi iPSCs
neurons
+ dox
lentiviral delivery of sgRNA
fluorescent Halo ligand
Selected KDs from Halo validation
non-tagged CRISPRi iPSCs
neurons
+ dox
lentiviral delivery of sgRNA
TDP-43 immuno-fluorescence
B
sgRNA
Halo-TDP-43
Merge + Lyso
NT
BORCS6 KD
20 µm
C
Significant compared to NT
Mean Halo Intensity (A.U.)
p <0.0001 except BORCS5 (p=0.0291)
NT
BORCS1 KD
BORCS2 KD
BORCS3 KD
BORCS4 KD
BORCS5 KD
BORCS6 KD
BORCS7 KD
BORCS8 KD
D
BORC
TARDBP
BORCS1
BORCS2
BORCS3
BORCS4
BORCS5
BORCS6
BORCS7
BORCS8
Screen
Halo Imaging
IF
-log10(p value)
LFC
E
Ubiquitin
TARDBP
CUL1
GID8
MAEA
NAE1
NEDD8
RANBP9
RMND5A
SAE1
SKP2
UBA2
UBA3
UBC
UBE2H
UBE2I
UCHL5
WDR26
Screen
Halo Imaging
IF
-log10(p value)
LFC
F
m6A
TARDBP
CNOT1
CNOT3
KIAA1429
METTL4
METTL14
METTL21A
METTL3
SFPQ
YTHDF1
YTHDF2
ZC3H13
ZC3H18
Screen
Halo Imaging
IF
-log10(p value)
LFC
G
Mitochondria
TARDBP
COX10
COX6B1
CPOX
DTYMK
FASTK
GRSF1
MFN2
MRPL39
NDUFA8
PITRM1
PMPCB
RPIA
UQCRC2
UQCRQ
Screen
Halo Imaging
IF
-log10(p value)
LFC

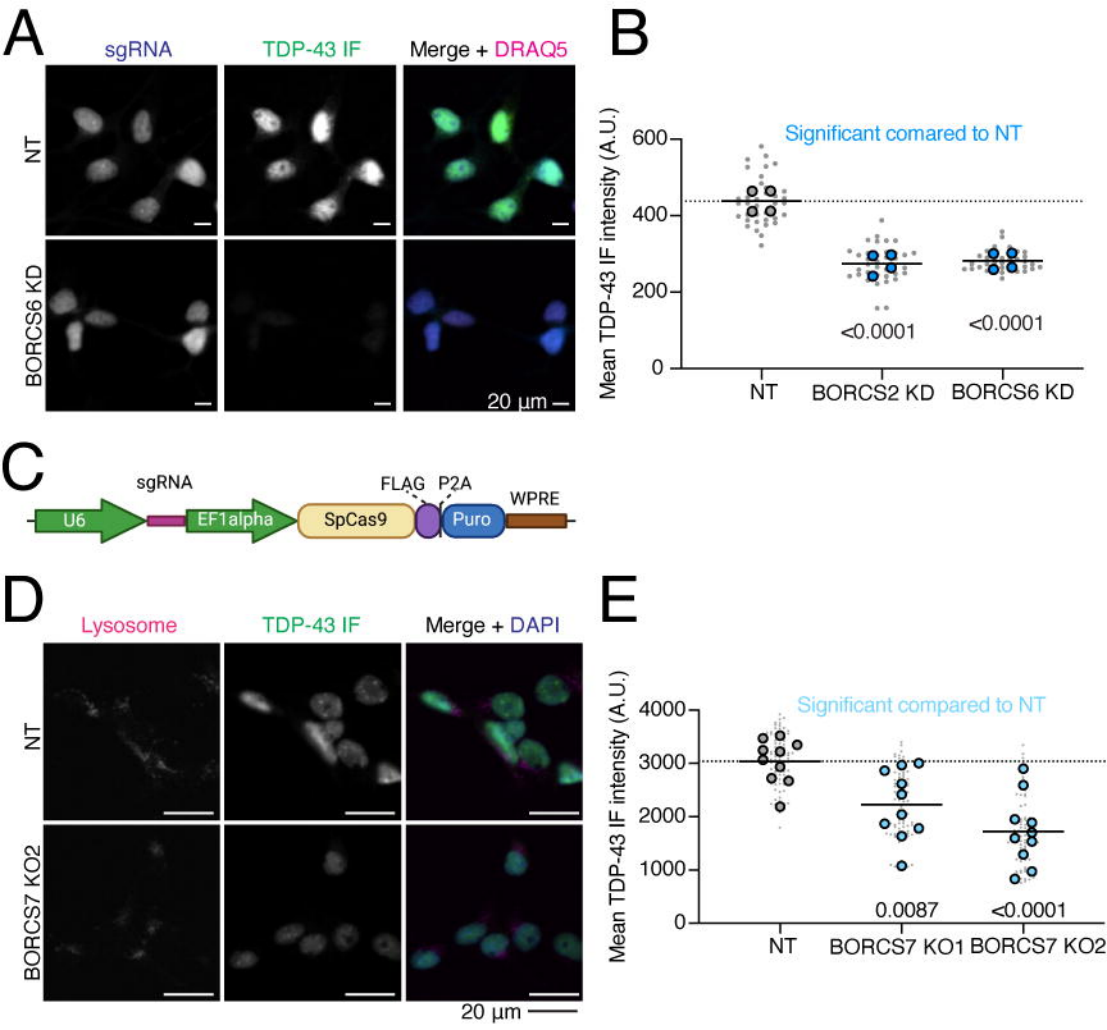
A
sgRNA
TDP-43 IF
Merge + DRAQ5
NT
BORCS6 KD
20 µm
B
Significant comared to NT
Mean TDP-43 IF intensity (A.U.)
600
400
200
0
<0.0001
<0.0001
NT
BORCS2 KD
BORCS6 KD
C
sgRNA
FLAG
P2A
WPRE
U6
EF1alpha
SpCas9
Puro
D
Lysosome
TDP-43 IF
Merge + DAPI
NT
BORCS7 KO2
20 µm
E
Significant compared to NT
Mean TDP-43 IF intensity (A.U.)
4000
3000
2000
1000
0
0.0087
<0.0001
NT
BORCS7 KO1
BORCS7 KO2

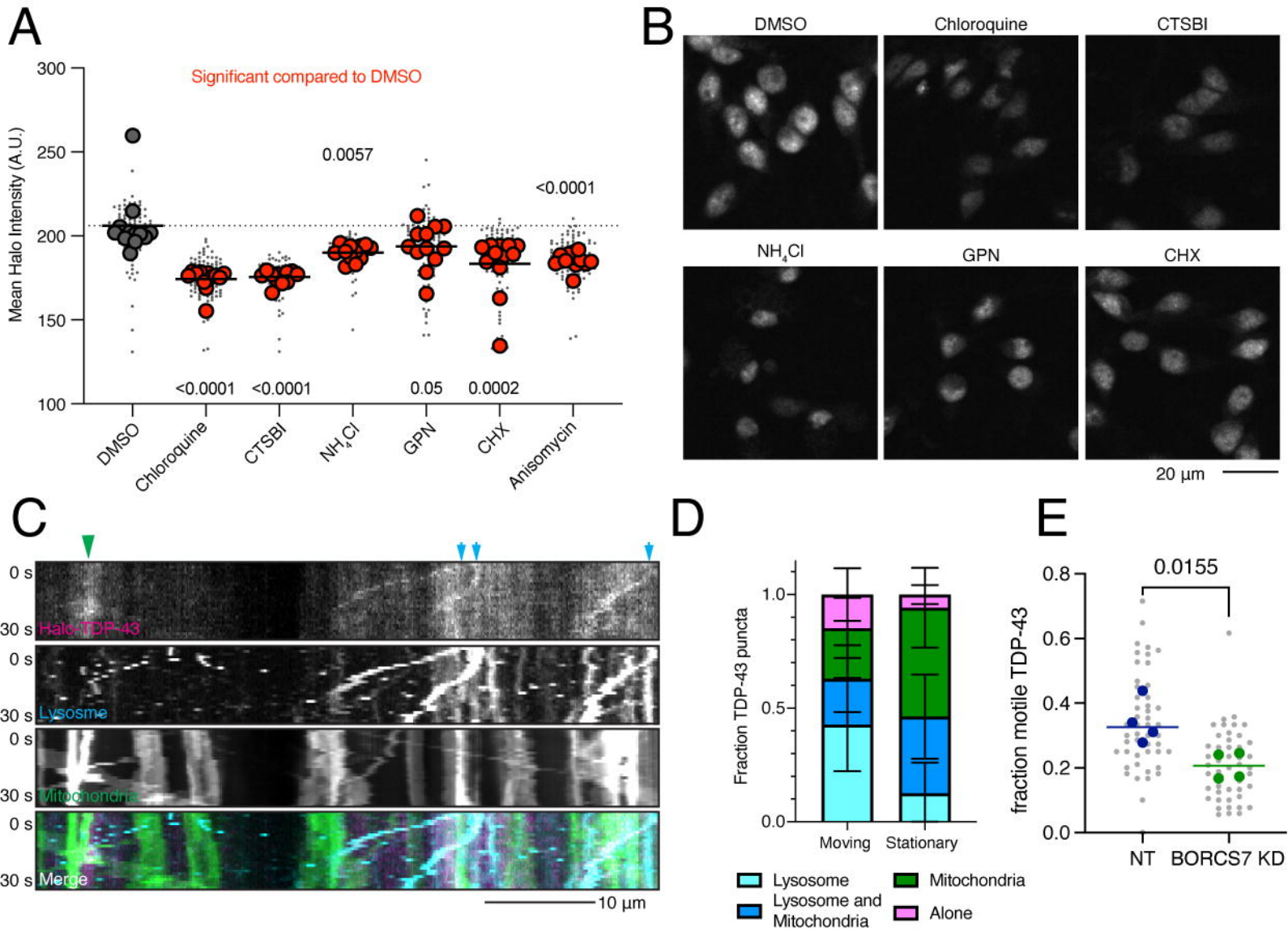
A
Significant compared to DMSO
Mean Halo Intensity (A.U.)
300
250
200
150
100
0.0057
<0.0001
<0.0001
<0.0001
0.05
0.0002
DMSO
Chloroquine
CTSBI
NH4Cl
GPN
CHX
Anisomycin
B
DMSO
Chloroquine
CTSBI
NH4Cl
GPN
CHX
20 µm
C
0 s
30 s
Halo-TDP-43
Lysosome
Mitochondria
Merge
10 µm
D
Fraction TDP-43 puncta
1.0
0.5
0.0
Moving
Stationary
Lysosome
Lysosome and Mitochondria
Mitochondria
Alone
E
0.0155
fraction motile TDP-43
0.8
0.6
0.4
0.2
0.0
NT
BORCS7 KD

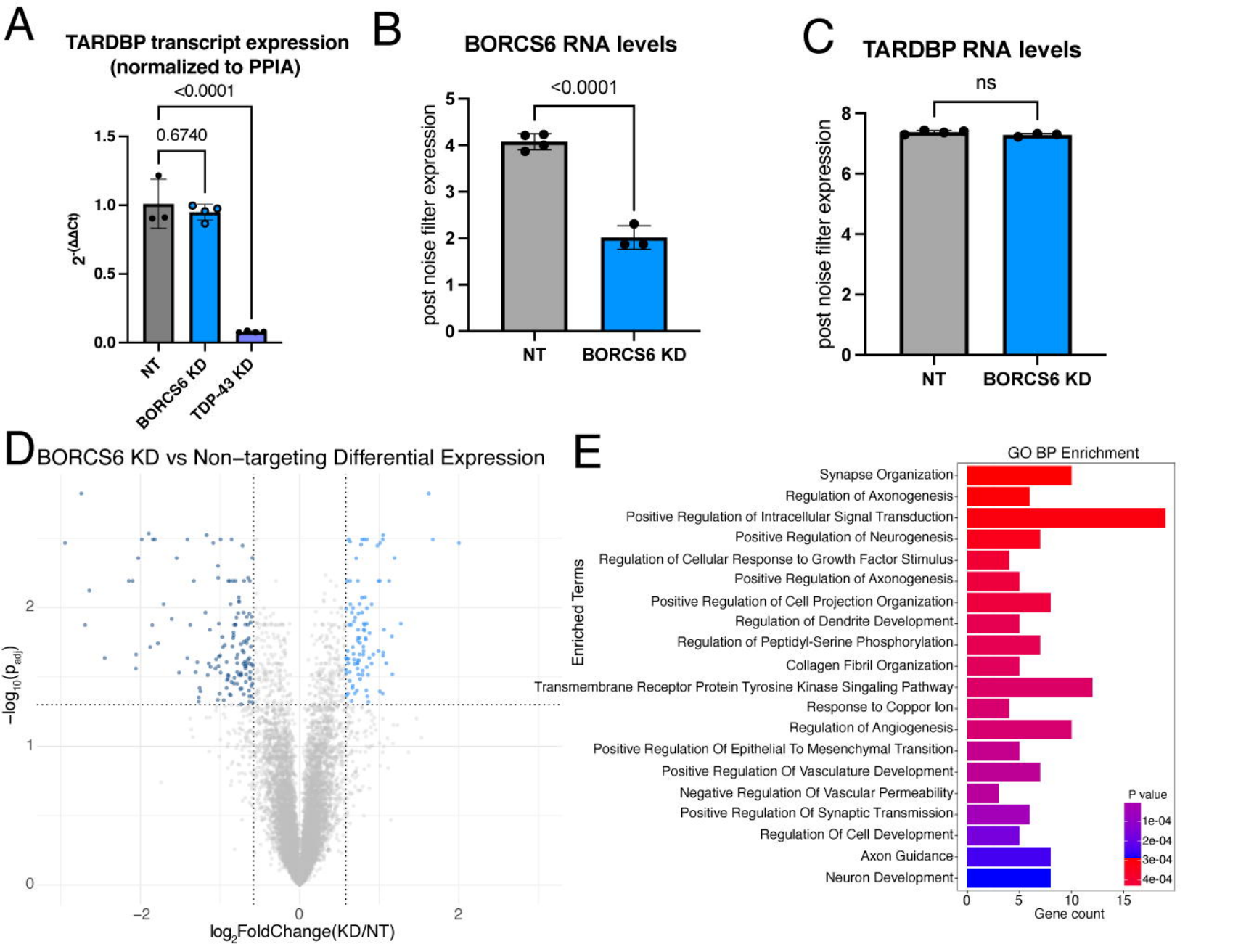
A
TARDBP transcript expression (normalized to PPIA)
<0.0001
0.6740
2^-(ΔΔCt)
1.5
1.0
0.5
0.0
NT
BORCS6 KD
TDP-43 KD
B
BORCS6 RNA levels
<0.0001
post noise filter expression
5
4
3
2
1
0
NT
BORCS6 KD
C
TARDBP RNA levels
ns
post noise filter expression
8
6
4
2
0
NT
BORCS6 KD
D
BORCS6 KD vs Non−targeting Differential Expression
−log10(padj)
2
1
0
−2
0
2
log2FoldChange(KD/NT)
E
GO BP Enrichment
Enriched Terms
Synapse Organization
Regulation of Axonogenesis
Positive Regulation of Intracellular Signal Transduction
Positive Regulation of Neurogenesis
Regulation of Cellular Response to Growth Factor Stimulus
Positive Regulation of Axonogenesis
Positive Regulation of Cell Projection Organization
Regulation of Dendrite Development
Regulation of Peptidyl-Serine Phosphorylation
Collagen Fibril Organization
Transmembrane Receptor Protein Tyrosine Kinase Singaling Pathway
Response to Coppor Ion
Regulation of Angiogenesis
Positive Regulation Of Epithelial To Mesenchymal Transition
Positive Regulation Of Vasculature Development
Negative Regulation Of Vascular Permeability
Positive Regulation Of Synaptic Transmission
Regulation Of Cell Development
Axon Guidance
Neuron Development
P value
1e-04
2e-04
3e-04
4e-04
0
5
10
15
Gene count

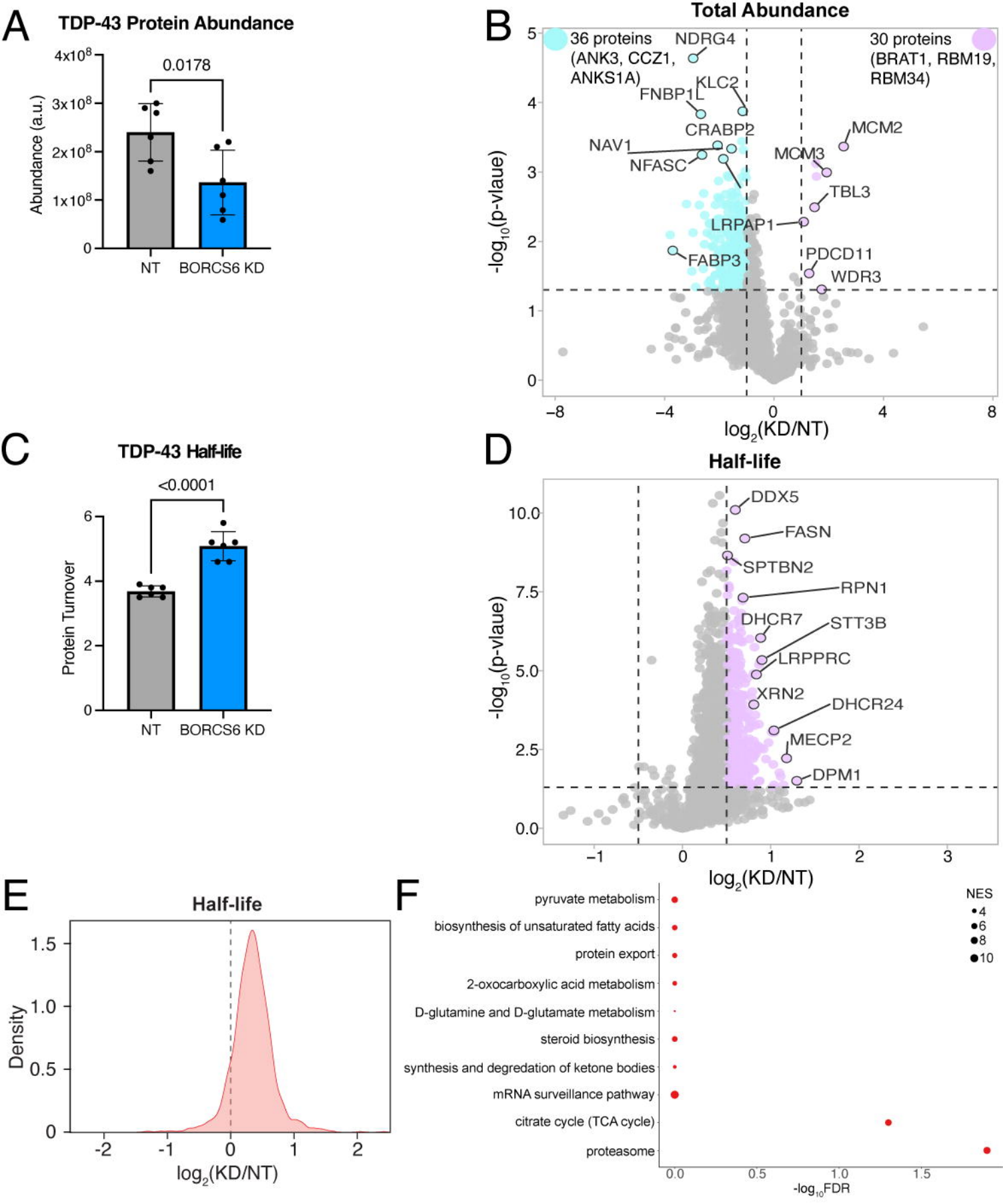
A
TDP-43 Protein Abundance
0.0178
Abundance (a.u.)
4x10^8
3x10^8
2x10^8
1x10^8
0
NT
BORCS6 KD
B
Total Abundance
36 proteins (ANK3, CCZ1, ANKS1A)
30 proteins (BRAT1, RBM19, RBM34)
NDRG4
KLC2
FNBP1L
CRABP2
NAV1
NFASC
MCM2
MCM3
TBL3
LRPAP1
FABP3
PDCD11
WDR3
-log10(p-vlaue)
log2(KD/NT)
C
TDP-43 Half-life
<0.0001
Protein Turnover
NT
BORCS6 KD
D
Half-life
DDX5
FASN
SPTBN2
RPN1
DHCR7
STT3B
LRPPRC
XRN2
DHCR24
MECP2
DPM1
-log10(p-vlaue)
log2(KD/NT)
E
Half-life
Density
log2(KD/NT)
F
pyruvate metabolism
biosynthesis of unsaturated fatty acids
protein export
2-oxocarboxylic acid metabolism
D-glutamine and D-glutamate metabolism
steroid biosynthesis
synthesis and degredation of ketone bodies
mRNA surveillance pathway
citrate cycle (TCA cycle)
proteasome
NES
-log10FDR